



**HAL**  
open science

# Near-Bed Sediment Transport Processes During Onshore Bar Migration in Large-Scale Experiments: Comparison With Offshore Bar Migration

Florian Grossmann, David Hurther, Joep van der Zanden, Agustín Sánchez-arcilla, José M Alsina

► **To cite this version:**

Florian Grossmann, David Hurther, Joep van der Zanden, Agustín Sánchez-arcilla, José M Alsina. Near-Bed Sediment Transport Processes During Onshore Bar Migration in Large-Scale Experiments: Comparison With Offshore Bar Migration. *Journal of Geophysical Research. Oceans*, 2023, 128 (3), pp.e2022JC018998. 10.1029/2022jc018998 . hal-04040908

**HAL Id: hal-04040908**





**<https://hal.science/hal-04040908>**

Submitted on 22 Mar 2023

**HAL** is a multi-disciplinary open access archive for the deposit and dissemination of scientific research documents, whether they are published or not. The documents may come from teaching and research institutions in France or abroad, or from public or private research centers.

L'archive ouverte pluridisciplinaire **HAL**, est destinée au dépôt et à la diffusion de documents scientifiques de niveau recherche, publiés ou non, émanant des établissements d'enseignement et de recherche français ou étrangers, des laboratoires publics ou privés.

## Near-Bed Sediment Transport Processes During Onshore Bar Migration in Large-Scale Experiments: Comparison With Offshore Bar Migration

Florian Grossmann<sup>1</sup> , David Hurther<sup>2</sup>, Joep van der Zanden<sup>3,4</sup> , Agustín Sánchez-Arcilla<sup>1</sup> , and José M. Alsina<sup>1</sup> 

<sup>1</sup>Universitat Politècnica de Catalunya, Barcelona, Spain, <sup>2</sup>Laboratory of Geophysical and Industrial Flows (LEGI), CNRS, University Grenoble Alpes, Grenoble INP, Grenoble, France, <sup>3</sup>Maritime Research Institute Netherlands, Wageningen, The Netherlands, <sup>4</sup>Water Engineering and Management Department, University of Twente, Enschede, The Netherlands

### Key Points:

- Migration results from balance of onshore-directed, short-wave related bedload and offshore-directed, current-related suspended transports
- From storm to recovery waves there is change to onshore migration because stronger reduction in offshore- than onshore-directed transports
- Streaming and infragravity wave influences are visible but negligibly low; wave breaking and nonlinearity influences are more important

### Correspondence to:

F. Grossmann,  
florian.grossmann@upc.edu

### Citation:

Grossmann, F., Hurther, D., van der Zanden, J., Sánchez-Arcilla, A., & Alsina, J. M. (2023). Near-bed sediment transport processes during onshore bar migration in large-scale experiments: Comparison with offshore bar migration. *Journal of Geophysical Research: Oceans*, 128, e2022JC018998. <https://doi.org/10.1029/2022JC018998>

Received 21 JUN 2022  
Accepted 2 MAR 2023

**Abstract** Detailed information on nearshore sediment transport processes during onshore bar migration were obtained from large-scale laboratory experiments with bichromatic wave groups on a relatively steep initial beach slope (1:15). Detailed measurements of velocity and sand concentration near the bed from shoaling up to the outer breaking zone including suspended sediment and sheet flow transport are presented. The analysis focuses on onshore migration under an accretive wave condition but comparison to an erosive condition highlights important differences. Decomposition shows that total transport mainly results from a balance of short wave-related, bedload onshore transport and current-related, suspended offshore transport. When comparing the accretive to the more energetic erosive condition, the balance shifts toward onshore transport, and onshore migration, because the short wave-related transport does not decrease as much as the current-related transport. This is related to the effects of skewness and asymmetry combined with less sediment suspension in the water column and undertow magnitude under the accretive condition. Transports from streaming in the wave boundary layer and from infragravity waves become visible but only play a subordinate role. Identified priorities for numerical model development include parametrization of wave nonlinearity effects and better description of wave breaking and its influences on sediment suspension.

**Plain Language Summary** Nearshore sandbars are seabed features that protect coastal infrastructure behind many sandy beaches around the world. In response to waves they change in shape and distance to the beach. To improve understanding of their onshore and offshore movement (migration), experiments representing natural conditions in a controlled laboratory setting were done. In this context, the underwater transport of sand was measured on the basis of flow velocities and sediment concentration in the water. The most important factors for migration direction were: shape of the waves (asymmetries about horizontal and vertical axes), wave breaking and resulting flows, and processes to lift sediments into the water column and keep them suspended. Under storm waves, the breaking-induced flows dominated the sediment transport so that bars moved offshore. In calmer conditions, the shape of the waves dominated the transport so that bars moved onshore. The inherent complexities of these processes make their mathematical replication difficult, as shown by comparison to literature. Consequently, priorities for advancing the forecasting of sandbar movement, improving coastal protection, were identified.

## 1. Introduction

Nearshore sand bars are alongshore ridges on the seabed, typically located in the shoaling and surf zones of many beaches around the world (e.g., Wijnberg & Kroon, 2002; Wright & Short, 1984). They can be alongshore uniform or feature complex geometries like rip channels and crescentic shapes (e.g., van Enckevort & Ruessink, 2003b). In regards to the predominant mechanism of their formation, the breakpoint hypothesis, originally proposed by Dyhr-Nielsen and Sørensen (1970) and demonstrated via numerical modeling by Dally and Dean (1984), is widely accepted. There, the bars form via convergence of onshore transport from bedload under shoaling waves and offshore transport from suspended transport under broken waves—thus being located close to the points of wave breaking. Through wave breaking bars promote energy dissipation. As a consequence, less wave energy reaches the shoreline, reducing erosion and storm damage. Additionally, bars play an important role

© 2023. The Authors.

This is an open access article under the terms of the [Creative Commons Attribution-NonCommercial-NoDerivs License](https://creativecommons.org/licenses/by/4.0/), which permits use and distribution in any medium, provided the original work is properly cited, the use is non-commercial and no modifications or adaptations are made.

for the nearshore sediment budget and coastal management strategies like nourishments (e.g., Kroon et al., 1995; van Duin et al., 2004).

Bar onshore and offshore migration is an inherent characteristic of transitions between beach states (Wright & Short, 1984), often with changes to their shape and sand volume. Offshore migration, occurring during transitions toward dissipative beaches, is typically associated with highly energetic events (e.g., Kuriyama, 2002) leading to large migration velocities (e.g., Ruessink et al., 2007; van Enckevort & Ruessink, 2003a). Under persistent (repetitive in time over long time intervals) wave action in the laboratory, bars were observed to migrate offshore until quasi-equilibrium between the profile and the hydrodynamics was reached (e.g., Eichtopf et al., 2018). Under field conditions they have been observed to keep migrating offshore until dissipating at the outer edge of the morphologically-active zone (e.g., Kuriyama, 2002; Walstra et al., 2012). Onshore migration, occurring during transitions toward reflective beaches, has been observed during changes to milder wave conditions (e.g., Gallagher et al., 1998; Ruessink et al., 2007)—typically associated with post-storm periods. Note that onshore migration velocities are generally much lower (e.g., van Enckevort & Ruessink, 2003a), which complicates observations and partly explains the relatively low number of field and laboratory observations available (Eichtopf et al., 2018). In the present experimental campaign, persistent hydrodynamics in the laboratory produced either a bar migrating until quasi-equilibrium between profile and hydrodynamics, or a dissipating bar (e.g., Eichtopf et al., 2020). Observations in the field highlighted welding of the bar to the beach (e.g., Phillips et al., 2017; Ruiz de Alegría-Arzaburu & Vidal-Ruiz, 2018). A better understanding of migration would help to align engineering solutions with natural recovery processes (e.g., Baldock & Alsina, 2013).

Competing sediment transport processes are the cause of bar migration. Undertow is a time-averaged, offshore-directed current mainly associated with suspended offshore transport (e.g., Gallagher et al., 1998; Roelvink & Stive, 1989). It originates from onshore water mass transports and radiation stress gradients, which originate from wave breaking (e.g., Svendsen, 1984), and continuously transports the sand, mainly put into suspension by short wave action, in the offshore direction. Near-bed streaming within the wave boundary layer (WBL) is a time-averaged current which has been associated with onshore and offshore transport (e.g., Kranenburg et al., 2012). It tends to be of comparatively low magnitude but acts on the high sediment concentrations near the bed. Onshore streaming contributions originate from a wave-averaged downward transport of horizontal momentum, which originates from the bed's influence on the phase of horizontal and vertical orbital velocities (Longuet-Higgins, 1953). Offshore streaming contributions originate from non-zero wave-averaged turbulent shear stresses which originate from differences in intrawave turbulence at different phases of the wave (e.g., Ribberink & Al-Salem, 1995; Trowbridge & Madsen, 1984).

Onshore transport is often related to wave asymmetries, the deviations from the simple sinusoidal waveshape assumed in linear wave theory. During propagation in the shoaling zone, interactions with the bed promote non-linear energy transfers between different frequencies (e.g., Hasselmann et al., 1963), particularly to super-harmonic components, increasing crests while broadening troughs (skewness; asymmetry about the horizontal axis). The larger crest than trough velocities then lead to more efficient sediment entrainment and transport under crests (e.g., Ruessink et al., 2011). Toward the breaking point, non-linear energy transfers also lead to changes in the phasing between harmonics, causing asymmetry about the vertical axis (saw-tooth shape of waves, e.g., Elgar & Guza, 1985; Flick et al., 1981). As a result, there are larger accelerations at upcrossings compared to downcrossings. There are various explanations as to how this causes onshore transport; smaller WBL thickness and consequently larger bed shear stress under the wave crest (Nielsen, 1992) being a prominent one. Furthermore, deviations from the classical assumption that sediment grains react quasi-instantaneously to hydrodynamic forcing, so called “phase-lag” or time history effects, should also be mentioned. They have been shown to considerably affect sheet flow transport rates for fine sands, high velocities and short wave periods (Dohmen-Janssen et al., 2002).

Once sediment has been entrained, the balance between settling under the action of gravity and upward movement under advective-diffusive processes determines suspension and mixing characteristics. Diffusive mixing (or gradient diffusion) may be described as small scale vertical exchanges which tend to transport sediment upwards because concentrations at lower elevations are higher (e.g., Nielsen, 1992, p. 202 for a detailed explanation). This kind of process is often characterized via so-called sediment diffusivity (e.g., Nielsen, 1992), regularly assumed equal or linearly-related to turbulent (eddy) viscosity of the fluid (e.g., Thorne et al., 2009). Advective (convective) mixing occurs when sediment is trapped in vortices (e.g., Tooby et al., 1977). They

often form near the bed by fluid interaction with the bed (bedforms) and get ejected at flow reversal (e.g., Amoudry et al., 2013; Bagnold, 1946; Thorne et al., 2002), sometimes reaching high elevations above the bed (e.g., Williams et al., 2007). Additionally, wave breaking has been observed to inject turbulence into the water column (e.g., Cox & Kobayashi, 2000; Sumer et al., 2013; Zhou et al., 2017), potentially influencing diffusive processes via its effects on turbulent viscosity (e.g., Deigaard et al., 1986). Furthermore, sediment pumping (Villard et al., 2000), potentially through the build-up of turbulence over consecutive short waves in a group (e.g., Holmedal et al., 2004; Kassem et al., 2015), has been observed as a process of sediment suspension under wave groups (e.g., van der Zanden et al., 2019b).

The physical processes (i.e., time-averaged currents, waves asymmetries and sediment mixing) behind sediment transport and bar migration have been described in various works at different degrees of complexity. However, especially during bar onshore migration events, their implications and roles are still not clear. Several authors have related differences in bar migration direction (onshore/offshore) to wave asymmetry (e.g., Henderson & Allen, 2004; Hoefel & Elgar, 2003; Hsu et al., 2006). Yet, most of such studies compare numerical modeling with beach profile evolution and no relations to detailed sediment transport measurements have been shown, to our best knowledge. Furthermore, numerical modeling in this context has been shown to heavily depend on calibration (e.g., Dubarbier et al., 2015; Rafati et al., 2021) to account for physical processes either not understood or not modeled.

The complexity of measuring sediment transport during onshore bar migration is high. This is because concentrations, from very low in suspension (accessible with standard instrumentation) to very high near the bed (multiple order of magnitude difference; not accessible with standard instrumentation), must be measured over the long periods of time required for onshore bar migration to occur. The present study aims to improve the knowledge of detailed sediment transport processes during recovery events characterized by onshore bar migration. To highlight important differences, a comparison with previously analyzed processes during storm events characterized by offshore bar migration is made. Section 2 introduces the experimental setup and data treatment. Section 3 summarizes results on morphological evolution, hydrodynamic quantities (wave heights, velocities, skewness and asymmetry) and sediment transport within the sheet flow layer and above. Subsequently, the results are discussed and put into context with similar studies (Section 4) to form conclusions (Section 5).

## 2. Experimental Setup and Data Analysis

The present data were acquired within the HYDRALAB+ transnational access project “Influence of storm sequencing and beach recovery on sediment transport and beach resilience” (RESIST). Details of the experimental protocol and data analysis were already presented in Eichentopf et al. (2020) and Grossmann et al. (2022). Therefore, only the most important aspects will be repeated here.

### 2.1. Facility and Test Conditions

The experiments were conducted in the large-scale CIEM wave flume at the Universitat Politècnica de Catalunya (UPC) in Barcelona. The flume is 100 m long, 3 m wide, and 4.5 m deep, and is equipped with a wedge-type wave paddle. The cross-shore coordinate  $x$  was defined as 0 at the wave paddle, increasing toward the beach. The absolute vertical coordinate  $z$  refers to still water level (SWL, Figure 1) while the bed-referenced coordinates  $\zeta$  and  $\zeta'$  refer to the seabed and point upwards.  $\zeta$  accounts for continuous bed evolution throughout the tests, establishing the same vertical reference system for all ensembles measured during a test (being the bed elevation during the first velocity upcrossing of each ensemble).  $\zeta'$  additionally references each measurement to the instantaneous bed elevation at which it was measured, ensuring that time-averaging and frequency filtering do not consider values below this elevation. For more details on the vertical reference systems, see Grossmann et al. (2022). The flume contained medium-grained sand with a median sediment diameter ( $D_{50}$ ) of 0.25 mm and a measured still water settling velocity  $w_s$  of 0.034 m/s.

Bichromatic (to facilitate frequency separation) erosive (E1 and E2) and accretive (A1, A2, and A3) waves were applied in three different sequences (Table 1). This article focuses on the low energy, accretive wave condition A1 ( $H_{rms} = 0.23$  m) while comparison to the higher energy erosive wave condition E2 ( $H_{rms} = 0.32$  m) will also be presented. They are termed accretive and erosive because of their dimensionless sediment fall velocities  $\Omega_{rms, A1} = \frac{H_{rms}}{T_p * w_s} = 1.44$  and  $\Omega_{rms, E2} = 2.54$  (e.g., Wright & Short, 1984). All A1 testing sequences with

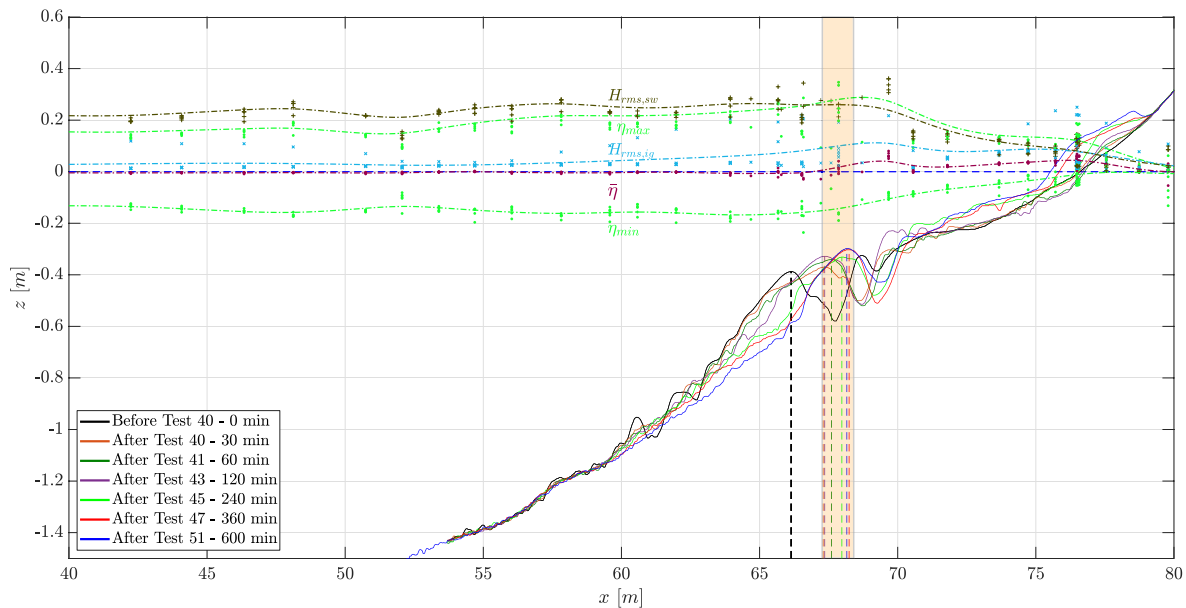


**Figure 1.** Example of morphological (profile) evolution in selected, consecutive A1 tests within storm sequence 1 of RESIST. SWL in dark blue dashed and profiles after tests 39 (E2), 40 (A1), 41 (A1), 43 (A1), 45 (A1), 47 (A1), and 51 (A1) in different colors. Time-averaged water levels and short wave and infragravity wave heights with points measured in each test plotted as markers and smoothing spline interpolation to obtain line. Identified bar maxima as dashed vertical lines and all visually observed breakpoints under A1 within shaded area.

onshore-migrating bars started from a well-developed outer breaker bar formed during previous high energy tests with E1 or E2 (Eichentopf et al., 2020). Throughout testing, bars were characterized by flat beds without ripples. Detailed information on hydrodynamics, morphological evolution and sediment transport under E2 were already presented in Grossmann et al. (2022). The present publication explains accretive processes while identifying similarities and differences to erosive processes, explaining the causes for different morphological evolution.

Primary frequency components in A1 were  $f_1 = 0.2276$  Hz and  $f_2 = 0.1979$  Hz (and  $H_2 = 2 \cdot H_1$ , see Table 1 in Eichentopf et al. (2020) for more detailed information). Their wave group period ( $T_g$ ) is defined as  $T_g = \frac{1}{f_1 - f_2} = 33.67$  s and there were 7 short waves per group. The waves were characterized by a primary mean period of  $T_p = \frac{1}{f_p} = 4.7$  s where  $f_p = \frac{f_1 + f_2}{2}$ . The repetition period ( $T_r$ ), that is, the period after which a wave phase repeated exactly, contained three slightly differing, alternating wave groups so that  $T_r = 3 \cdot T_g = 101.01$  s. In this study,  $T_r$  was of central importance because it determined the exact repetition of processes and the period for ensemble-averaging.

## 2.2. Instrumentation

The primary measurements were taken from a mobile frame which was re-positioned horizontally at intervals to measure in various locations surrounding the outer breaker bar. The Acoustic Concentration and Velocity Profiler (ACVP; Hurther et al., 2011) measured sediment concentrations, velocities and instantaneous bed elevations below the mobile frame. The co-located sediment concentration and velocity measurements (cross-shore and vertical) were provided as vertical profiles (1.5 mm bin size) of up to 20 cm above the seabed. Additional concentration measurements inside the ACVP measuring domain were obtained from a three-nozzle Transverse Suction System (TSS) on the mobile frame (used for measurement validation). Above the ACVP measuring domain, two Optical Backscatter Sensors (OBSs) were used to measure sediment concentrations at 40 Hz.

**Table 1**  
Wave Sequences in RESIST, Origin of Representative A1 Tests Shaded

| Sequence | Test number | Wave condition | Duration [min] | $\Omega$ [-] |
|----------|-------------|----------------|----------------|--------------|
| 1        | 16          | B              | 30             | 2.21         |
|          | 17–23       | E1             | 240            | 3.34         |
|          | 24–35       | A1             | 600            | 1.44         |
|          | 36–39       | E2             | 120            | 2.54         |
|          | 40–51       | A1             | 600            | 1.44         |
|          | 52          | B              | 30             | 2.21         |
| 2        | 53–56       | E2             | 120            | 2.54         |
|          | 57–68       | A1             | 600            | 1.44         |
|          | 69–74       | E1             | 240            | 3.34         |
|          | 75–86       | A1             | 600            | 1.44         |
| 3        | 87          | B              | 30             | 2.21         |
|          | 88–91       | E1             | 240            | 3.34         |
|          | 92–104      | A2             | 780            | 1.05         |
|          | 105–108     | E2             | 120            | 2.54         |
|          | 109–132     | A3             | 1440           | 0.72         |



Three-component outer flow velocities (i.e., higher than 10 cm from the bed) were measured at 100 Hz using a vertical array of three Nortek Vectrino Acoustic Doppler Velocimeters (ADV). The lowermost ADV was located within the ACVP measuring domain, approximately 10–15 cm above the seabed. The other two mobile frame ADVs were located approximately 20–25 cm and 30–35 cm above the seabed respectively. Water surface elevations were measured at 40 Hz using Resistive (wire) Wave Gauges (RWGs), Acoustic Wave Gauges (AWGs) and Pressure Transducers (PTs; conversion following Bonneton (2018)) in fixed locations along the flume. Additionally, one PT was attached to the mobile frame. Active beach profile transects were measured in intervals of 30 (60) minutes with a mechanical profiler. The measurements were conducted along the center line of the flume with a cross-shore resolution of 0.02 m and a vertical measuring accuracy of 0.01 m.

### 2.3. Data Treatment

The same data cleaning and averaging procedures as explained in Grossmann et al. (2022) were applied. Time-averaged sediment transport rates were calculated from beach profile transect measurements using the Exner equation (e.g., Baldock et al., 2011). The ACVP supplies profiles of acoustic backscatter intensity and sediment concentration information can be derived following the methodology of Hurther et al. (2011). This is done by iterating downwards from the emitter while accounting for the signal attenuation occurring along the way, as described in detail by Fromant et al. (2018). This requires certain calibration constants which represent hardware and particle backscattering characteristics. They were chosen separately for the two wave conditions because the different suspension conditions (i.e., overall lower sediment concentrations under accretive waves) required different system-dependent settings. However, the constants only varied slightly and were applied equally in all their tests. As a result, satisfying agreement of ACVP measurements with TSS time-averaged concentration measurements and net transport rates from the Exner equation was found in all tests considered here. Tests where air bubbles entrained from breaking waves (e.g., Cáceres et al., 2020) affected more than 5% of the time series (visible as acoustic backscattering amplitude drop-outs) were not considered. In accepted tests the influence from air bubbles was assumed negligible since ACVP saturation results in signal drop-out.

Sediment fluxes,  $q$ , from ACVP and OBS/ADV were calculated and decomposed as described in Grossmann et al. (2022). For transport rates,  $Q$ , depth-integrals were calculated at every instant of  $T_r$  over the total vertical domain available from ACVP, OBS, and ADV. For bedload net transport rates, instantaneous erosion depths and upper sheet flow limits (based on the 8%-volumetric criterion (Dohmen-Janssen et al., 2001) were used as integration boundaries (both boundaries within the ACVP measuring domain). For suspended load net transport rates, upper sheet flow limits and the upper ends of the domain available from ACVP, OBS, and ADV were used as integration boundaries. Instantaneous transport was time-averaged for most analyses and, for conciseness in the present publication, the “time-averaged” (or sometimes “net”) was omitted in most references to transport.

Data from multiple tests under the same wave condition were aggregated to provide a cross-shore resolution of detailed measurements around the onshore- and offshore-migrating bars. This was done by normalizing the cross-shore location of measurements from the mobile frame with the location of visually-identified bar crests (as in Grossmann et al. (2022)). The normalization is based on the assumption that in all considered tests of a certain wave condition the same type of morphological evolution (described in the following section) operates. This was confirmed by careful profile evolution analysis (not shown for brevity; see also Grossmann et al. (2022)) which showed that relative rather than absolute cross-shore coordinates determined bed evolution. It also showed that profiles in the considered tests had a very similar shape in the vicinity of the outer bar crest (3.5 m offshore and onshore of it), that bars had similar heights and similar freeboard.

## 3. Results

### 3.1. Morphological Evolution

Figure 1 exemplifies the morphological changes occurring under successive A1 tests. They were characterized by onshore migration of the outer bar ( $65 < x < 69$  m; bar crest cross-shore positions indicated with vertical dashed lines) with steepening of its offshore slope and reduction of the distance between SWL and bar crest. The outer bar features a pronounced bar trough. The inner bar ( $69 < x < 73$  m) slightly changes in shape and, overall, moves onshore at a similar speed as the outer bar so that the cross-shore distance between them stays constant. Additionally, the volume of sand within the outer bar slightly decreases whereas the volume of sand within the

inner bar increases. While the bars were characterized by a flat seabed, further offshore a tendency toward bed ripples becomes visible. Accretion is observed at the shoreline ( $x > 75$  m), resulting in the growth of a berm. The described morphological evolution was observed in all A1 tests presented here.

A1 accretive wave conditions will be compared to E2 erosive wave conditions. Application of E2 led to formation of an outer breaker bar and a smaller, inner breaker bar. The bars migrated offshore until a quasi-equilibrium between beach profile and hydrodynamics was reached—typical under erosive wave conditions as observed in many laboratory (e.g., Baldock et al., 2011; Eichentopf et al., 2018; van der Zanden et al., 2017b; van Rijn et al., 2011) and field experiments (e.g., Aagaard et al., 2008; Gallagher et al., 1998; Mariño-Tapia et al., 2007). For further analyses of the morphological changes under E2 and their causes, see Eichentopf et al. (2019) and Grossmann et al. (2022).

## 3.2. Hydrodynamics

### 3.2.1. Wave Heights

Figure 1 also shows the cross-shore evolution of water surface elevation quantities during A1. Onshore of the outer bar, the short waves' amplitudes (as indicated by  $H_{rms,sw}$ ,  $\eta_{min}$ , and  $\eta_{max}$ ) decrease, indicating wave breaking. The infragravity wave amplitude,  $H_{rms,ig}$ , increases slightly but stays constant throughout most of the surfzone. Offshore of the breakpoint there is a set-down and onshore of it a set-up. Like the changes in wave height, this is closely related to and caused by wave breaking. The measured maximum  $H_{rms,sw}$  and  $H_{rms,ig}$  are 40%–50% larger under E2 (Grossmann et al., 2022). Set-down and set-up, however, are of similar magnitudes and cross-shore evolutions.

### 3.2.2. Time-Averaged Velocities

Figure 2 shows the cross-shore evolution of time-averaged velocity measurements from the mobile frame and visually identified breakpoints under wave conditions E2 and A1. Beach profiles under the respective wave conditions were ensemble-averaged and the time-averaged velocities are shown in cross-shore position relative to the bar crest ( $x'$ ), rather than absolute cross-shore position ( $x$ ). Good agreement between ACVP and ADV measurements becomes visible (Figure 2a/b).

Offshore of the bar crest ( $x' < -1$  m), all A1 tests feature near-bed ( $\zeta < 0.05$  m) time-averaged onshore velocities—probably caused by a dominance of progressive wave streaming over wavelike streaming (e.g., Kranenburg et al., 2012; Longuet-Higgins, 1953). The largest near-bed time-averaged onshore velocities were measured on the bar's offshore slope (Figure 2c,  $-2 < x' < -1$  m). The erosive wave condition E2 does not feature time-averaged onshore velocity near the bed at those positions (e.g., Figure 2c, Test 39 at  $x' = -1.5$  m). In fact, under E2 time-averaged onshore velocity was only observed much further offshore and at 50% of the maximum magnitude measured under A1 (Figure 2a/c,  $x' = -2.8$  m).

As the bar crest is close to the breakpoint, undertow magnitudes increase during wave onshore propagation (Figure 2d) and for both wave conditions the largest undertow magnitudes were measured close to the bar crest ( $x' = -0.4$  m). Both wave conditions produced plunging breakers, with larger intensity in terms of aerated area, plunging and noise under E2. This is consistent with A1 featuring 20%–40% lower undertow magnitudes than E2 and 35% lower deep water wave power (or energy flux;  $P = E \cdot c_g$ ). Note that, due to the limited cross-shore resolution of detailed measurements, there is uncertainty over the position of maximum undertow velocity magnitude, which seems to be shifted further onshore under A1 than E2. In certain locations (e.g., Figure 2b,  $x' = -0.4$  m), time-averaged velocities opposing over  $z$  become visible. This is in line with the widely-accepted idea of near-shore circulation under breaking ocean waves—driven by onshore transport at high elevations through wave nonlinearity and rollers, and compensated by time-averaged offshore currents (undertow) near the bed (e.g., Svendsen, 2005).

### 3.2.3. Intrawave Hydrodynamics and Sediment Dynamics

Figure 3 presents ensemble-averaged measurements resolving  $T_r$  in a single A1 test 0.4 m offshore of the bar crest (see Grossmann et al. (2022) for similar plots under E2). During  $T_r$ , three wave groups occur (delimited by vertical dashed lines in the figure). Short wave amplitudes are much larger than infragravity wave amplitudes (Figure 3a) and the infragravity waves appear to be bound to the short waves (e.g., Baldock, 2012)—with largest infragravity troughs occurring during the highest short waves.

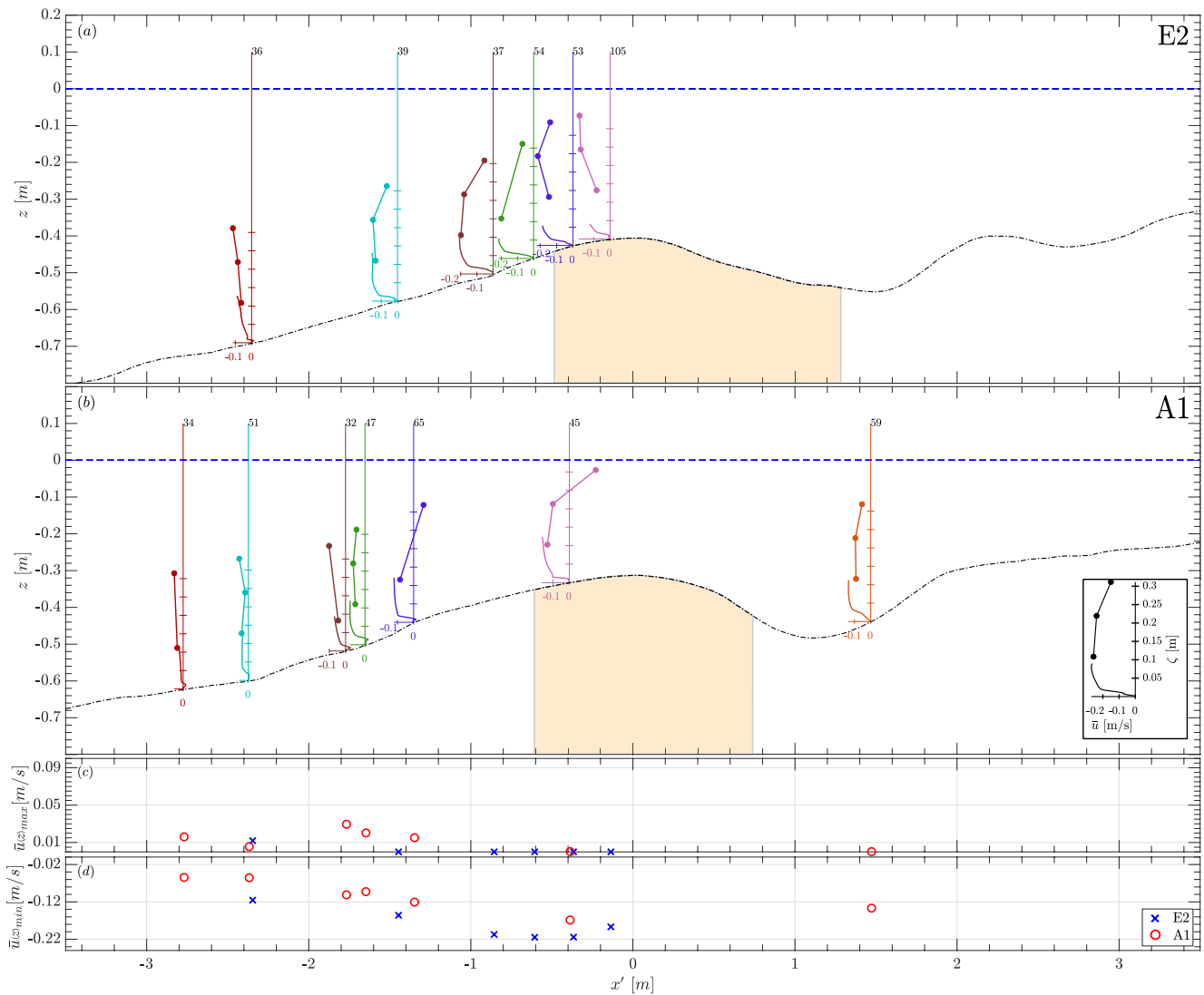


**Figure 2.** Time-averaged velocities in cross-shore positions relative to bar crest. Horizontal velocity profiles (same scaling) under wave conditions E2 (a) and A1 (b) from Acoustic Concentration and Velocity Profiler (ACVP) (near-bed solid lines; mini-axes ticks as shown in sketch in bottom right corner of (b)) and Acoustic Doppler Velocimeters (ADVs) (dots connected by solid lines) over ensemble-averaged beach profile (dashed-dotted black line) with still water level (dashed dark blue line). Respective test-averaged outer breaking locations  $\pm$  one standard deviation (shaded area); (c) Maximum (over vertical) of time-averaged onshore velocity measured by ACVP near the bed; (d) Maximum (over vertical) of time-averaged offshore velocity measured by ACVP and ADVs.

Ensemble-averaged, co-located measurements of  $u_\infty$  (measured at  $\zeta = 0.05$  m) show good agreement between ACVP and ADV as well as little deviation between the ensembles considered for ensemble-averaging (Figure 3b). Despite larger wave height,  $u_\infty$  magnitudes were similar under E2 (cf. Figure 7b in Grossmann et al. (2022)). This might be related to the lower water depths under A1. Furthermore, the present  $u_\infty$  time series appears asymmetry-dominated, with large time-dependent gradients (accelerations) of  $u_\infty$  at phases of upcrossings and smaller crest than trough magnitudes in the largest short waves. Further offshore (test 65 at  $x' = -1.4$  m, not shown for brevity), the time series still appears skewness-dominated, with the broad troughs and sharp crests (of higher magnitudes than in test 45) characteristic of higher order Stokes waves. Between  $x' = -1.4$  m and  $x' = -0.4$  m (shown in Figure 3) asymmetries in the largest short waves increased until breaking was initiated (e.g., Padilla & Alsina, 2017). Vertical,  $w_\infty$ , and infragravity,  $u_{ig}$ , velocities are much lower than  $u_\infty$ . Near-bed vertical gradients of  $u_\infty$  in contrast to approximately depth-uniform velocities at higher elevations become visible (Figure 3c). Near-bed velocities slightly lead the free-stream velocities at flow reversal (e.g., Figure 3c at  $t/T_r = 0.3$ —observe the difference in transition from offshore (blue) to onshore (yellow) velocity which occurs earlier at  $\zeta = 0.045$  m than  $\zeta = 0.005$  m), which is typical for oscillatory boundary layers (e.g., Jensen et al., 1989; Sleath, 1987; van der A et al., 2011).



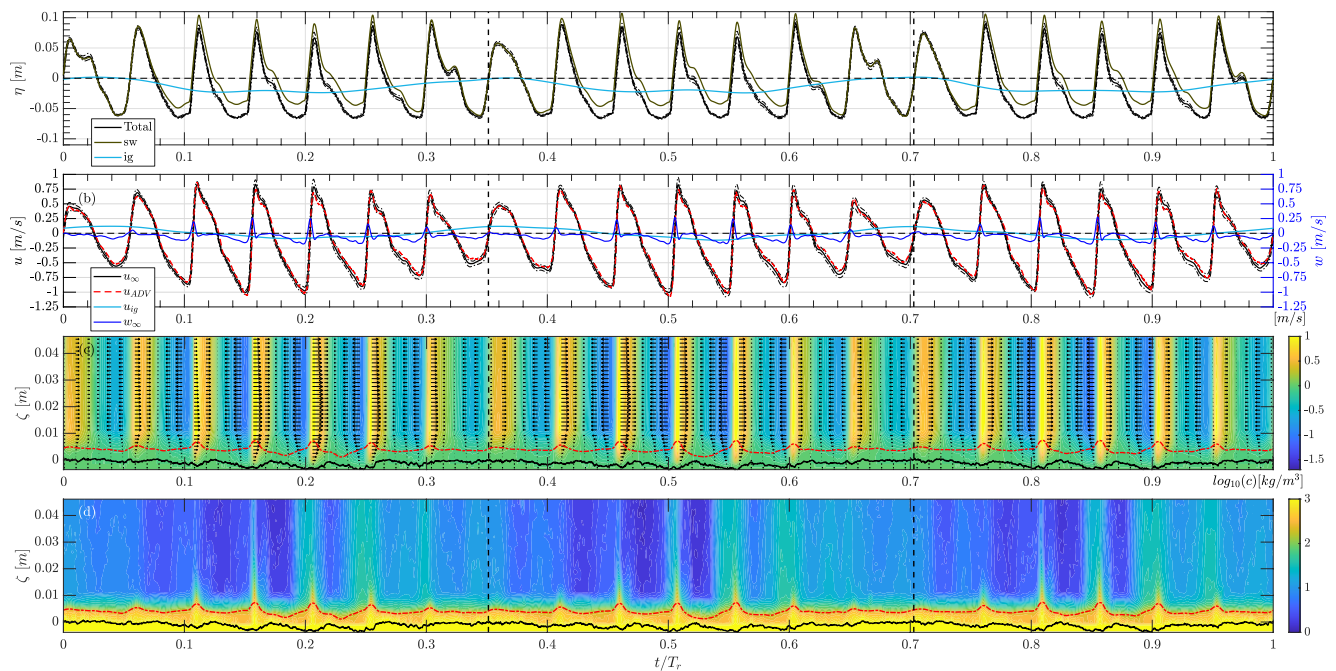


**Figure 3.** Ensemble-averaged hydrodynamic and sediment dynamics data in test 45 at  $x' = -0.4$  m (0.4 m offshore of the bar crest). Vertical dashed lines indicate separation into wave groups. (a) Water surface elevations from PT shown before (black line with  $\pm$  one standard deviation as black dashed-dotted line) and after separation into short wave (dark green) and infragravity contributions (light blue); (b) Free-stream velocities from Acoustic Concentration and Velocity Profiler (ACVP) (featuring  $\pm$  one standard deviation as black dashed-dotted line in  $u_\infty$ ) and lowest Acoustic Doppler Velocimeter, horizontal velocities referring to left y-axis and vertical velocity referring to right y-axis; (c) Near-bed velocity field from ACVP; (d) Near-bed concentration field from ACVP. Fields (c and d) referring to colorbars on their right and including instantaneous bed level (black) and upper limit of sheet flow layer (red dashed-dotted).

The main sediment suspension events occur simultaneously with the largest short wave crests (Figure 3d, e.g., at  $t/T_r = 0.205$ ). They feature expansions of sheet flow layer (SFL) width (red dashed-dotted lines in panels c and d) with large suspended concentrations near the bed. The sediment suspension extends in plumes to higher elevations ( $\zeta > 0.045$  m) as well, albeit at decreasing concentration. Under the first short waves of each group (e.g.,  $t/T_r = \{0.06; 0.11; 0.16; 0.41; 0.46; 0.51; 0.76; 0.81; 0.86\}$ ) sediments largely settle down before suspension by subsequent waves. In the second halves of the groups (e.g.,  $t/T_r = \{0.25 - 0.35; 0.55 - 0.7; 0.9 - 0.05\}$ ), however, suspended sediments seem to not settle down fully before re-suspension by subsequent short waves (see also Villard et al. (2000), O'Hara Murray et al. (2012), and van der Zanden et al. (2019b)). This indicates the importance of suspension or “storage” of sediment in the water column (e.g., Kobayashi, 2001) that might be advected. Consequently, the suspended sediments are not only transported in a quasi-instantaneous way but affected by time history effects. The increased suspension might be partly induced by larger velocity magnitudes and, most likely, by a build-up of turbulent kinetic energy in the water column over the duration of a wave group due to successive wave breaking (e.g., Larsen et al., 2020; van der Zanden et al., 2019a). In tests further offshore (not shown for brevity), fewer short waves lead to suspension events, the events are lower in vertical extent and magnitude, and tendency toward sediment re-suspension only becomes visible at  $x' = -1.4$  m and to a lesser degree.

When comparing intrawave time series at all mobile frame locations shown in Figure 2a/b, E2 featured  $u_\infty$  amplitudes 15%–25% larger than A1. At  $x' = -2.4$  m sediment suspension under E2 reached a few cm higher up in the water column but, under A1, it was more concentrated near the bed and of higher magnitude. At  $-1.7 \leq x' \leq -1.5$  m suspension plumes have similar magnitudes near the bed and reach the upper end of the measuring domain ( $\zeta \approx 0.12$  m) under both wave conditions. However, under E2 the sediment has a larger tendency to stay in suspension and intervals with no suspension between single short waves are much shorter (one third). At  $x' = -0.4$  m sediment stays in suspension throughout the whole  $T_r$  under E2 but only in the second half of  $T_g$  under A1. The SFL width (distance between instantaneous erosion depth and upper sheet flow limit) increases under both wave conditions while approaching  $x' = -0.4$  m. There, they are both estimated to have sheet flow occurring in roughly 6.5% of  $T_g$ . Nevertheless, E2 features a 20% higher SFL width, partly because of deeper bed erosion (higher maximum orbital velocities).

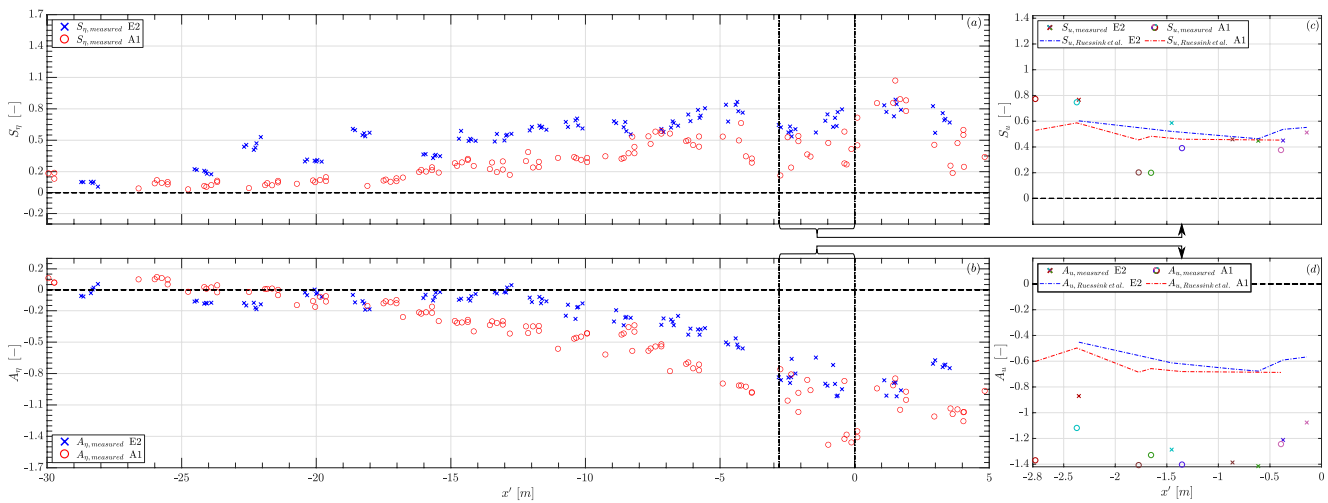


**Figure 4.** Water surface elevation skewness (a) and asymmetry (b) along the wave flume (bar crest-referenced coordinate  $x'$ ). Free-stream velocity skewness (c) and asymmetry (d) in vicinity of bar crest as measured at  $\zeta' = 0.05$  m (crosses and circles, colors indicating test number as shown previously) and predicted by the parametrization of Ruessink et al. (2012) (dashed-dotted lines).

### 3.2.4. Skewness and Asymmetry

Skewness and asymmetry are commonly used to account for natural waves' deviation from the perfectly sinusoidal shape assumed in linear wave theory. High-pass filtered (as described in Section 2.3) horizontal free-stream velocities  $u_{sw}$  and water surface elevation measurements  $\eta_{sw}$  (omitting PT measurements close to the bar crest where waves get very nonlinear) were input into:

$$S_{\xi} = \frac{\overline{\xi_{sw}(t)^3}}{\sigma_{\xi_{sw}}^3} \quad (1)$$

to calculate skewness  $S_{\xi}$  (with  $u$  and  $\eta$  substituted for  $\xi$  to indicate velocity and surface elevation skewness), which represents the waves' asymmetry about the horizontal axis. Here the overline represents time-averaging and  $\sigma$  is the standard deviation. To calculate asymmetry  $A_{\xi}$ , which represents the waves' asymmetry about the vertical axis,  $\xi_{sw}$  in the previous equation was replaced with its Hilbert transform (Elgar, 1987). As a result, waves with pitched-forward shape have negative  $A_{\xi}$ . Velocity asymmetries will be compared with the parametrization of Ruessink et al. (2012). Based on an empirical fit to 30,000+ field observations under non-breaking and breaking wave conditions, the parametrization provides skewness and asymmetry as a function of local significant wave height,  $H_s$ , local water depth,  $d$ , and wave period  $T$ .

Figure 4a shows an increase in  $S_{\eta}$  during propagation toward the bar crest.  $A_{\eta}$  (Figure 4b) increases as well but stays negligibly low for longer and does not show as much scatter to lower values. These results are in good agreement (not shown) with field data (e.g., Doering & Bowen, 1995; Ruessink et al., 2012) where a similar evolution was observed over increasing Ursell numbers (which tend to increase during onshore propagation over sloping (barred) profiles when waves become more nonlinear). E2 shows a tendency toward higher  $S_{\eta}$  than A1 while A1 shows a tendency toward higher  $A_{\eta}$  than E2. Close to the bar, and onshore of it, the nonlinearities under E2 and A1 become very similar—partly because of the increased scatter in measured values. Interestingly, A1 shows a distinct  $S_{\eta}$  peak onshore of the bar ( $1 < x' < 2$  m), consistent with wave breaking (e.g., Babanin et al., 2007). Under E2 there is a less clear peak at  $x' = -4$  m which, in conjunction with the undertow maximum at  $-0.6 \leq x' \leq -0.4$  m (Figure 2a/d), indicates initiation of breaking offshore of the bar.

Linear transfer of surface elevations to free-stream horizontal velocities is often assumed in practice and is supported by experimental evidence (e.g., Rocha et al., 2017; Zou et al., 2003). In this context,  $S_u$  and  $A_u$  (Figure 4c/d) support the higher skewness in E2 and higher asymmetry in A1 observed from surface elevations ( $\eta$ ). The parametrization captures  $S_u$  fairly well but tends to underestimate  $A_u$ . Furthermore, it provides very similar values under E2 and A1.

Note that Ruessink et al. (2012) do not recommend their parametrization for slopes larger than 1:30, like the present experiments' initial slope of 1:15, and rapid local profile changes, like the breaker bar at  $x' = 0$  m. Furthermore, the present tests had high Ursell numbers, ranging between 1.2 and 3. This is the upper end of wave nonlinearity considered in the data of Ruessink et al. (2012) and considerable scatter becomes visible in the related data (see Figure 1 in Ruessink et al. (2012)).

### 3.3. Sediment Concentration and Transport

#### 3.3.1. Time-Averaged Concentration

Figure 5 shows profiles of time-averaged sediment concentration at selected relative cross-shore locations. Near the bed, the ACVP provided profiles of high vertical resolution. Certain tests feature shorter vertical extents because of larger morphological changes in the respective cross-shore location and because the ensemble with smallest vertical extent determined the vertical extent of the ensemble-average (as explained in detail in Grossmann et al. (2022)). The single data points at higher elevations originate from OBS measurements, vertically-interpolated as explained in Grossmann et al. (2022). To analyze processes of sediment suspension, Rouse profiles (black dashed lines) were fitted (nonlinear least squares fit) to the measured data:

$$\bar{C}(\zeta') = C_0 \left( \frac{z_a}{\zeta'} \right)^{\frac{1}{m}} \quad (2)$$

where  $C_0$  is the reference concentration measured at reference height  $z_a$  (0.015 m),  $m$  is a mixing parameter, based on profile shape and fitted to the measurements, describing vertical mixing processes (both  $C_0$  and  $m$  are reported in each panel) and the upper limit of the fit is  $\zeta' = 0.1$  m. Rouse profiles are based on the assumption that sediment in suspension only originates from vertical exchange, where upward turbulent diffusion is balanced by downward settling. All tests show a large vertical gradient of multiple orders of concentration magnitude near the bed ( $\zeta' < 0.015$  m). Most tests show a rapid transition to a smaller, and seemingly depth-constant (in the semi-log plot), gradient at larger elevations above the bed. The fits are observed to capture the profile shapes very well.

Under both wave conditions, the measured time-averaged concentrations generally increase while approaching  $x' = -0.4$  m (Figure 5). At  $x' = -2.4$  m (panels a and d), A1 shows larger  $C_0$  (factor 2.25) but lower suspended concentrations (factor 1.64 at  $\zeta' = 0.05$  m) than E2. At  $-1.7 \leq x' \leq -1.5$  m (panels b and e), E2 shows larger  $C_0$  (factor 3.83) and suspended concentrations (factor 4 at  $\zeta' = 0.05$  m). At  $x' = -0.4$  m (panels c and f), E2 shows larger  $C_0$  (factor 2.28) and larger suspended concentrations (factor 2 at  $\zeta' = 0.05$  m). Thus, apart from locations very far offshore and near the bed, E2 always features considerably higher (factor 1.64–4) time-averaged suspended concentrations than A1. The mixing parameter  $m$  indicates similar mixing processes in most of the observed locations, despite larger energy under E2. Only far offshore under A1 (panel d) mixing is much weaker. Thus, the higher suspended concentrations under E2 are related to the larger entrainment (as indicated by  $C_0$ ) and availability of sediment for mixing into the water column. Mobility numbers  $\psi$ , calculated according to  $\psi = \frac{(A\omega)^2}{(s-1)gd_{50}}$  (e.g., Nielsen, 1992, p. 103) for every short wave and averaged subsequently, are consistent with the visual observation (Section 3.1) of flat beds with a tendency toward bed ripples further offshore under the less energetic wave condition A1 (Figure 5d).

#### 3.3.2. Linking Transports and Morphological Evolution Under A1

Figure 6 serves to connect the previously observed morphological evolution under A1 to sediment transport rates. As explained in Section 2.3, they can be calculated for each test over the entire active beach profile by inputting beach profile transect measurements into the Exner equation. Ensemble-averaging over all considered tests provides the red solid line shown in Figure 6. To quantify the influence of error accumulation in residuals and measurement inaccuracies, the calculations were repeated without correction for residuals and with a shift of profiler measurements by their inaccuracy (up and down 1 cm). This provides the error bounds (red dashed lines) shown in Figure 6. By depth-integrating and time-averaging ACVP and OBS/ADV instantaneous sediment flux measurements, total transport rates (circle markers) in the cross-shore locations of the mobile frame can be obtained. When comparing them to the transport from profile transect measurements, good agreement well within error bounds is observed.

There is onshore transport rate over the entire region surrounding the outer and inner bars (Figure 6). The onshore transport rate increases on the offshore side of the bar crests and decreases on their onshore side, with the

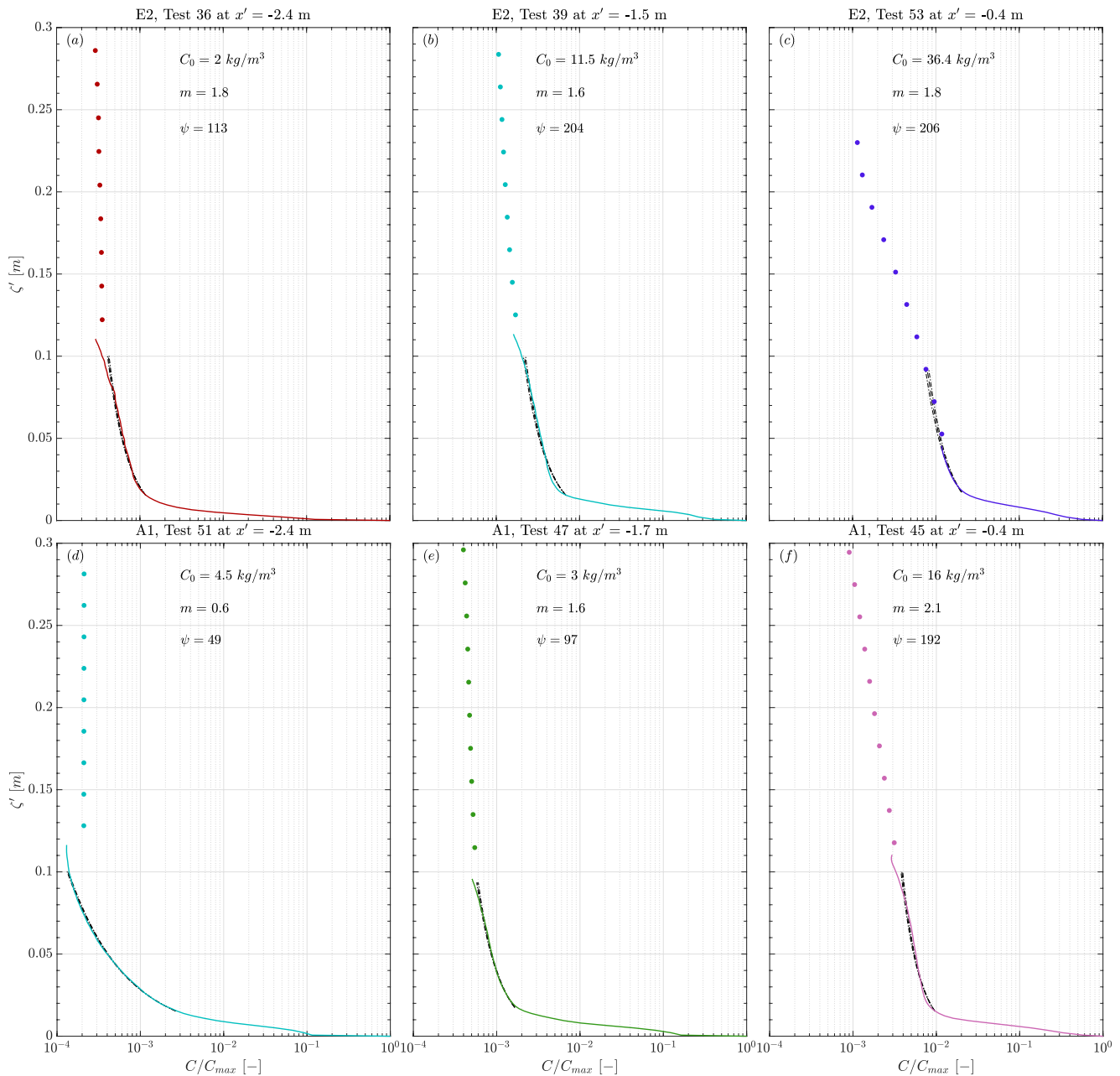


**Figure 5.** Time-averaged (over  $T_s$ ) sediment concentration profiles normalized with bed concentration,  $C_{max}$ , of  $1650 \text{ kg/m}^3$  from Acoustic Concentration and Velocity Profiler (ACVP) (near-bed solid lines) and OBSs (dots) under E2 (a–c) and A1 (d–f) over logarithmic horizontal axes in respective relative cross-shore positions. Fitted Rouse profiles of suspended sediment concentration (dashed black lines) with 95% confidence bounds (dashed-dotted black lines). Fitting parameters  $C_0$ , measured at  $z' = 0.015 \text{ m}$ , and  $m$ , from nonlinear least squares fit to data, and mobility number  $\psi$ , calculated as explained in Section 3.3.1, shown at top of each panel. Note that data of concentrations below  $0.165 \text{ kg/m}^3$  are not shown.

respective local maxima located slightly offshore of the crests and cross-shore changes in transport rate being very low. The present variations in transport rate indicate a distinct pattern of morphological evolution over the outer bar: Slight increase of onshore transport rate on the offshore side of the bar ( $x' < -0.5 \text{ m}$ ) results in erosion; slight decrease of onshore transport rate on the onshore side of the bar ( $x' > 0 \text{ m}$ ) results in accretion. At the same time, there is larger onshore transport rate on the offshore side of the bar ( $x' = -1 \text{ m}$ ) than on its onshore side ( $x = 1 \text{ m}$ ). In combination this leads to onshore migration of the bar, maintaining its general shape. In contrast, E2 featured offshore transport rate increasing on the offshore side of the bar crests followed by decreases on their onshore side, causing offshore bar migration (Grossmann et al., 2022).

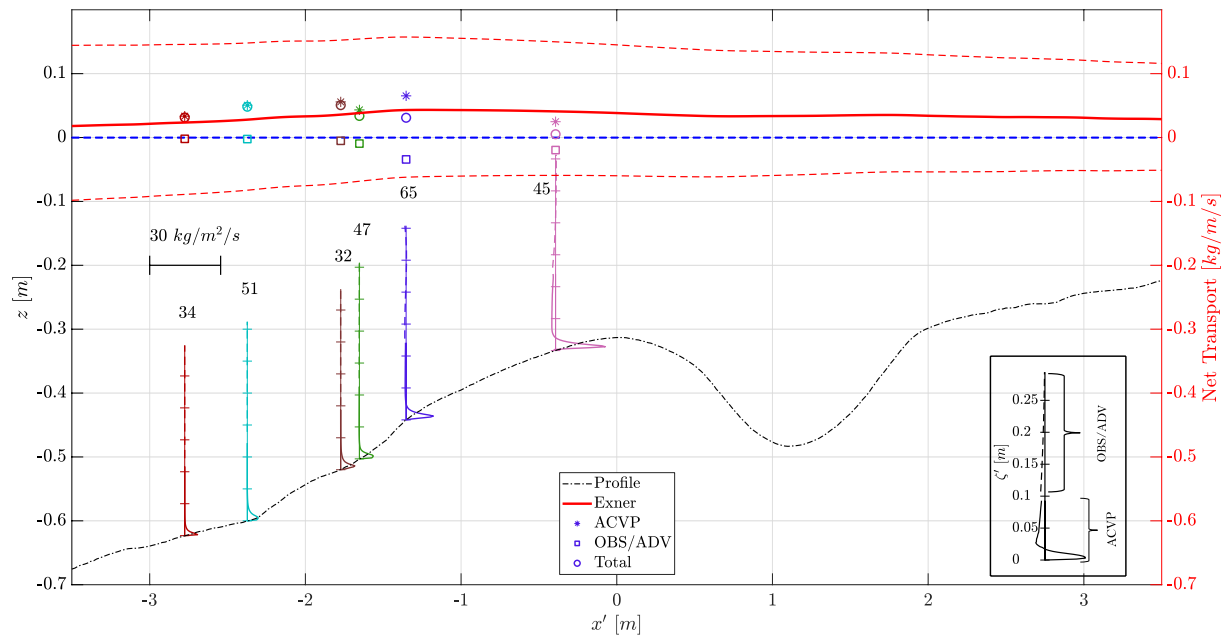


**Figure 6.** Net transport under A1 from mechanical profiler, Acoustic Concentration and Velocity Profiler (ACVP) and Optical Backscatter Sensor/Acoustic Doppler Velocimeter (OBS/ADV). Cross-shore evolution of net transport and comparison of net transport from the different methods. Profile transect measurements (red line referring to right y-axis) based on ensemble-averaging of Exner equation calculations in single tests with error bounds (red dashed lines) calculated as explained in accompanying text (Section 2.3). ACVP and OBS/ADV measurements (stars and squares with color indicating respective tests) are based on depth-integration and time-averaging of instantaneous measurements of horizontal velocity and sediment concentration in the  $\zeta'$ -coordinate system. They are shown separately and as their summation (circles). Additionally, depth-resolving net flux profiles from ACVP and OBS/ADV shown in their respective relative cross-shore positions with mini-axes according to sketch in the bottom right corner and scale as shown at  $x' = -3$  m.

### 3.3.3. Decomposed Sediment Fluxes

Resolving the vertical dimension of ACVP and OBS/ADV measurements (Figure 6; vertical profiles referring to mini-axes as shown in bottom right corner) provides additional detail on transport processes. Specific cross-shore locations were chosen for comparing (decomposed) sediment fluxes in A1 to E2 (Figures 7a–7f). Offshore of the bar ( $x' = -2.4$  m; panels a and d), onshore flux over a thin layer near the bed dominates (up to  $\zeta' = 0.015$  m in E2 and  $\zeta' = 0.035$  m in A1), with a 86% larger magnitude under E2. Closer to the bar ( $-1.7 \leq x' \leq -1.5$  m; panels b and e), the maximum near-bed onshore flux magnitudes increase under E2 and A1 (140% and 40% respectively when comparing to  $x' = -2.4$  m). The suspended offshore flux magnitudes under A1 do not increase as significantly as they do under E2. On the bar ( $x' = -0.4$  m; panels c and f), the maximum suspended offshore flux magnitudes under E2 and A1 increase (double and one order of magnitude respectively when compared to  $-1.7 \leq x' \leq -1.5$  m). But in contrast to E2, the maximum near-bed onshore flux magnitude under A1 increases (factor 3.5 compared to  $x' = -1.7$  m) instead of decreases (43% of the value at  $x' = -1.5$  m). Most likely, this is related to wave breaking positions. Under E2 waves already break offshore of the bar, leading to energy dissipation. Under A1 they break further onshore, shifting near-bed onshore flux maxima further onshore.

To explain how different time scale-related processes contributed to the observed total transports, sediment fluxes were Reynolds-decomposed (Figures 7g–7r; see Grossmann et al. (2022) for details on the decomposition, which neglects turbulent fluxes, and note that infragravity contributions were negligibly small). In all positions, the short wave-related flux profiles (panels g–l) are characterized by onshore contributions near the bed ( $\zeta < 0.045$  m). This onshore flux is driven by the skewed and asymmetric oscillatory flow, which leads to more developed sheet flow layers and higher transport rates during the crest phase than the trough phase (see also Section 3.2.3).

The current-related flux profiles (Figures 7m–7r) explain the differences between total and short wave-related flux profiles. Offshore of the bar ( $x' = -2.4$  m; panels m and p), there is onshore flux very close to the bed ( $\zeta' < 0.01$  m) due to streaming (see Section 3.2.2). Closer to the bar ( $-1.7 \leq x' \leq -1.5$  m; panels n and q) under A1 the same profile shape remains but, due to undertow, there is an increase in suspended offshore flux magnitude (factor 3 at  $\zeta' = 0.035$  m). E2, in contrast, features an entirely offshore-directed current-related flux



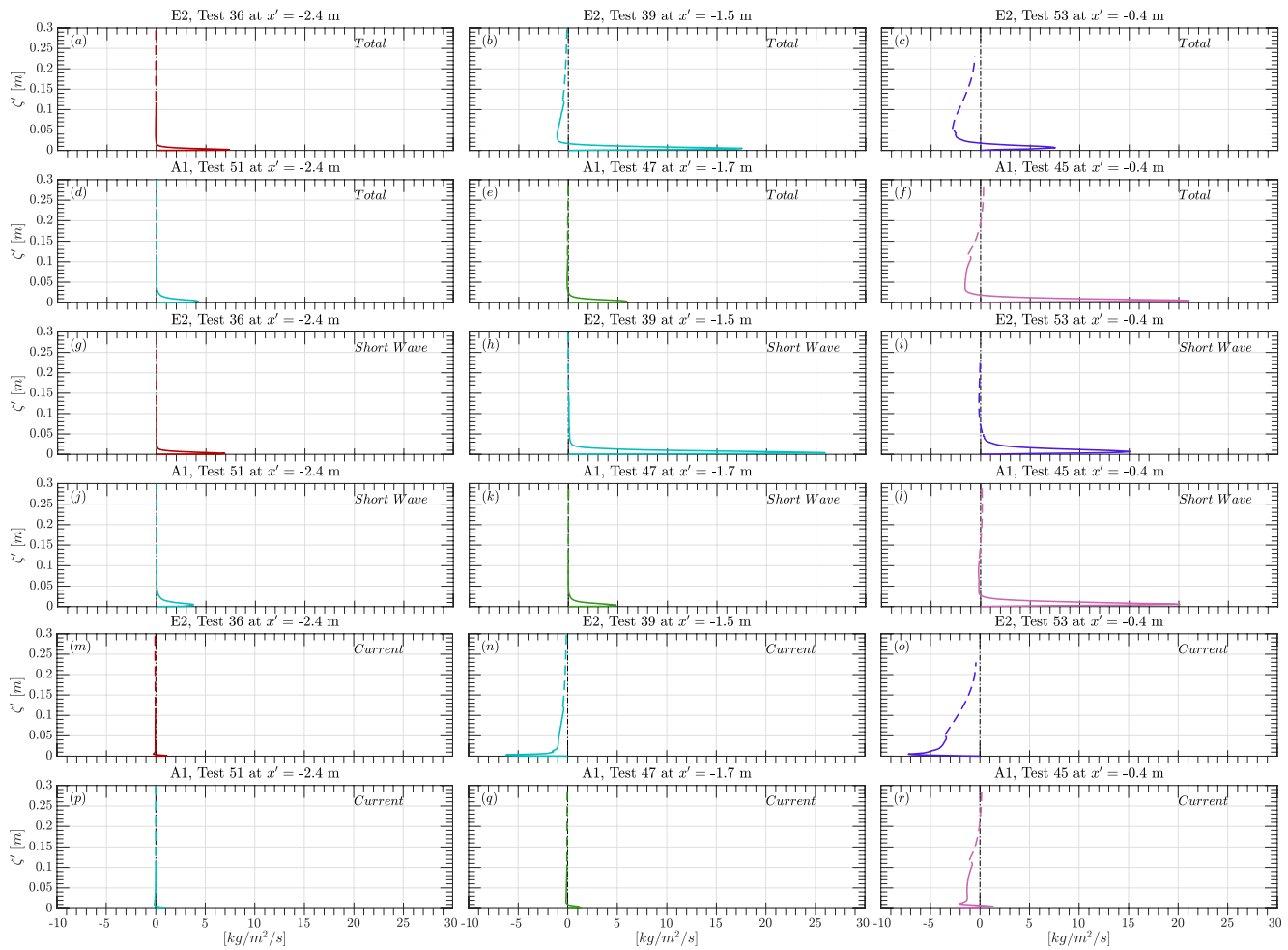


**Figure 7.** Selected decomposed net flux profiles under wave conditions E2 (a, b, c, g, h, i, m, n, o) and A1 (d, e, f, j, k, l, p, q, r). Panels on top of each other compare the two wave conditions at similar  $x'$  in total (a–f), short wave-related (g–l), and current-related (m–r) net flux.

profile with a maximum near the bed. On the bar ( $x' = -0.4$  m), under E2 (panel o) the vertical extent with large suspended offshore flux increases considerably (compared to  $x' = -1.5$  m) while the maximum magnitudes are very similar (only 16% larger). A1 (panel r) features a very distinct profile with offshore flux over the largest part of the water column, intercepted by a small onshore flux at  $\zeta = 0.005$  m and lower onshore fluxes at higher elevations ( $\zeta > 0.2$  m). This indicates a competition between onshore-directed streaming and offshore-directed undertow influences. Because of their comparably low magnitudes, the infragravity flux profiles were omitted.

### 3.3.4. Depth-Integrated Transport Rates

Vertical profiles of sediment fluxes are depth integrated over the whole domain available from ACVP and OBS/ADV and displayed in Figure 8. E2 features considerably larger magnitudes than A1 (note the changing y-axis ticks in panels a–d). While, under E2, onshore transport only becomes visible in the most offshore location ( $x' = -2.4$  m in panels a and c), total onshore transport was measured in all locations under A1 (panels b and d). Under both wave conditions transport from the infragravity wave-related component are small compared to the other components (panels a and b). Therefore, total transport mainly results from the balance of short wave- and current-related components.

Under E2 (Figure 8a), current-related offshore transport dominates onshore-directed short wave-related transport in all locations. Under A1 (Figure 8b), current-related transport is onshore-directed far from the bar ( $x' \leq -1.8$  m) and only become offshore-directed in its close vicinity ( $x' \geq -1.7$  m). The increase in current-related offshore transport between  $x' = -1.8$  m and  $x' = -0.4$  m is larger than the increase in short wave-related onshore transport.



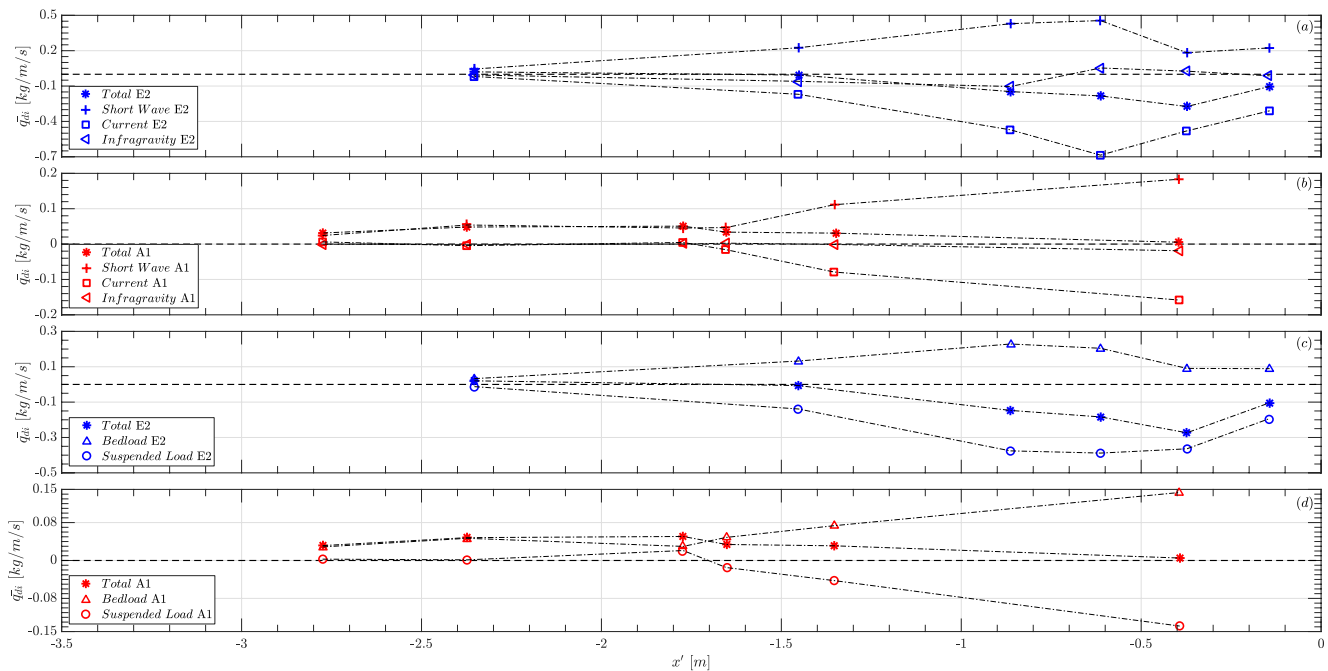


**Figure 8.** Cross-shore evolution of depth-integrated (over entire available vertical extent as shown in Figure 6), time-averaged sediment transport under wave conditions E2 (a and c) and A1 (b and d), decomposed by frequency (a and b) and vertically (c and d). Note the changing y-axis limits.

Nevertheless, the short wave-related component already features a considerable magnitude offshore ( $x' = -2.8$  m) which causes the total transport to be onshore-directed in all locations under A1. Toward  $x' > 0$  m the onshore transport steadily decreases and seems to approach a negative value, which would be in contrast to results from the Exner equation (Figure 6). This tendency might result from sediment suspended above the available measurement domain up to elevations above wave trough level (e.g., van der Zanden et al., 2017a)—which would result in an onshore contribution.

The transports were also decomposed vertically (Figure 8c/d) into bedload (vertically integrated over the sheet flow layer as explained in Section 2.3) and suspended load (vertically integrated from the top of the sheet flow layer to the maximum vertical elevation available as explained in Section 2.3). Interestingly, the cross-shore evolution of bedload (suspended) transport is very similar to the cross-shore evolution of short wave-related (current-related) transport under both wave conditions. Onshore transport predominantly occurs as bedload and offshore transport only occurs as suspended load. Under A1, the higher magnitudes of bedload transport result in total onshore transport while, under E2, the higher magnitudes of suspended transport result in total offshore transport.

## 4. Discussion

### 4.1. Accretive Morphological Evolution

Large-scale measurements of sediment dynamics during storm erosion and beach recovery have been presented. Energetic wave conditions produced a breaker bar with offshore migration toward the breakpoint location. An inner bar, also generated during the erosive condition, migrated similarly with the outer bar. Subsequent, milder wave energy conditions produced the onshore migration of both the outer and inner bars. This pattern of bar dynamics is consistent with previous laboratory and field measurements.

Eichentopf et al. (2018), analyzing data from earlier experiments, observed the pattern of bar dynamics under random waves in the CIEM with  $\Omega_{rms} = 1.22$  (cf. their Figure 3a). Furthermore, the pattern was re-produced in the smaller Scheldt flume (50 m length) under down-scaling of the same wave conditions (cf. Figure 12 in van Rijn et al. (2011)). Baldock et al. (2011) observed the pattern in the CIEM under monochromatic, bichromatic and random waves of the same energy flux but with  $\Omega_{rms} = 0.9$ ,  $\Omega_{rms} = 1.2$  and  $\Omega_{rms} = 1.1$  respectively (blue and

green lines in their Figure 7a, and black and red lines in their Figures 8a/9a). Yoon and Cox (2010) observed the pattern in the 104 m long wave tank at Oregon State University while replicating the well-known DUCK 94 field campaign (e.g., Gallagher et al., 1998) with random waves (estimated  $\Omega_{rms} = 1.2$ ; see their Figure 3b). Cheng and Wang (2018) observed the pattern in the field at the west-central Florida coast (see their Figure 9c).

However, as illustrated by Eichtopf et al. (2018), bar migration during low energy conditions is more complex than the single pattern of bar dynamics observed here. They identified in other experiments in the CIEM ( $\Omega_{rms} = 1.41$  and  $\Omega_{rms} = 1.06$ ) a different type of accretive morphological evolution where: “The secondary bar, ..., merges with the breaker bar.” and concluded that “...breaker bar evolution under accretive wave conditions cannot be condensed to a single pattern as under erosive wave conditions.” In this context, not only the hydrodynamics but also the initial beach configuration seemed important, influencing the breaking location and resulting sediment transport processes. Baldock et al. (2017) observed a similar importance of morphological hysteresis where the bar dynamics at the onset of low energy conditions influenced subsequent sediment transport and the final beach configuration. Other tests in RESIST (not shown here) featured other types of accretive morphological evolution and will be subject to future analyses.

## 4.2. Comparing Sediment Transport Processes

Morphological evolution is the result of sediment transport and related hydrodynamic processes. However, data on sediment transport under accretive conditions is even more scarce than data on profile evolution, partly because transport is more difficult to measure than profiles. Consistent with the present data, the other comparable studies (Mieras et al., 2019; van der Zanden et al., 2017a) stress that total transport magnitude mainly results from the balance between short wave-related, bedload onshore and current-related, suspended offshore transport. An advantage of the present experiments with fully-evolving beach profiles is the direct comparison between erosive wave conditions (E2), causing bar offshore migration, and accretive conditions (A1), causing bar onshore migration. Under A1 both short wave-related, bedload onshore and current-related, suspended offshore transport are lower than under E2. However, the reduction in current-related, suspended offshore transport was relatively larger, resulting in total onshore transport—consistent with bar onshore instead of bar offshore migration. This was linked to reduced undertow magnitude, sediment entrainment and mixing under A1.

### 4.2.1. Transport and Wave Asymmetries

Experiments have shown that increased asymmetry leads to increased transport of quasi-instantaneously reacting sand in propagation direction of waves (e.g., King, 1991; van der A et al., 2010). A similar relation holds for skewness, as long as phase lags effects (Ribberink et al., 2008) play a minor role (e.g., Dibajnia & Watanabe, 1992; O’Donoghue & Wright, 2004). This is consistent with the increase in short wave-related, bedload onshore transport (under E2 and A1) during propagation toward the bar (Figure 8).

Close to the bar, a decrease in short wave-related, bedload onshore transport became visible under E2. This is consistent with initiation of wave breaking (Section 3.2.4). Under A1, breaking occurred further onshore so that waves propagated deeper into the surf zone without reductions in energy and skewness. There, they acted on shallow water depths (which were already shallower under A1 compared to E2, cf. Figure 2a/b), potentially increasing short wave-related, bedload onshore transport further.

As visible from the present experiments and from literature (e.g., Doering & Bowen, 1995), the cross-shore evolution of wave nonlinearities in a bar’s vicinity is closely linked to wave breaking, and nonlinearities are closely linked to transport. Certain models (e.g., Torres-Freyermuth et al., 2010) already replicate the general cross-shore evolution of wave nonlinearity successfully and transport formulations under consideration of wave nonlinearity have been developed (e.g., Hoefel & Elgar, 2003; van der A et al., 2013). However, the many complexities of wave breaking still introduce large inaccuracies and modeling of nonlinear wave propagation is associated with large computational costs, stressing the need for easily applicable parametrizations.

### 4.2.2. Time-Averaged Velocities

Wave condition A1 features lower undertow magnitudes than E2 (Figure 2). In combination with lower sediment suspension (Section 4.2.3) this heavily contributes toward onshore migration of the bar (instead of offshore migration). In field experiments under comparable hydro-sedimentary conditions, Greenwood and Osborne (1990) observed an even larger post-storm reduction in undertow magnitude close to the outer bar crest. Thornton

et al. (1996) present field measurements of low undertow magnitudes over the outer bar before the onset of a storm. The main drivers of undertow are the mass and momentum flux between trough and crest level as well as radiation stress (vertical and cross-shore) and set-up (cross-shore) gradients (e.g., Svendsen, 1984). Therefore, large undertow magnitudes should only be expected when wave breaking and other influences produce large gradients in forcing. This normally happens in storms with large wave heights.

During offshore bar migration (storm conditions), accurate numerical modeling of undertow magnitudes has been shown with different models and under different assumptions (e.g., Christensen et al., 2002; Garcez Faria et al., 2000). During onshore bar migration, Lescinski and Özkan-Haller (2005) highlight some difficulties in undertow modeling (as well as its importance for replicating morphologies). In a recent study with a state-of-the-art model, Rafati et al. (2021) still show considerable inaccuracies in undertow modeled during bar onshore migration (see their Figure 3f), hindcasting opposite directions in certain cross-shore locations. Generally, there is a larger margin for error in undertow modeling during offshore bar migration since magnitudes are higher (so that small inaccuracies do not matter as much). Inaccuracies are introduced into the analysis because the complexity of governing equations requires simplifying assumptions and parametrizations of boundary conditions. Furthermore, the assumptions and parametrizations have mainly been validated under storm conditions, inherently assuming that they apply in accretive modeling as well—which may not be the case.

Interestingly, the present experiments show streaming near the bed, leading to time-averaged onshore velocities (Figure 2) and onshore flux (Figure 7). But since its vertical extent is very limited, its influence is much lower than undertow's (which acts over large parts of the water column). Next to process-based numerical models (e.g., Kranenburg et al., 2012), streaming has also been considered in semi-empirical transport formulations (e.g., Nielsen & Callaghan, 2003; van der A et al., 2013). However, in the present experiments its onshore contributions appeared far less important than the short wave-related contributions.

#### 4.2.3. Sediment Entrainment and Mixing

The entrainment of sediment is a very complex process under the influence of turbulence (e.g., Soldati & Marchioli, 2012). In practical applications, entrainment has often been related to near-bed velocities and critical bed shear stress in the form of Shields parameters (e.g., Nielsen, 1992, p. 222). However, experiments have also identified an influence of breaking-injected turbulence onto entrainment (e.g., Sumer et al., 2013; van der Zanden et al., 2017a). The present experiments show increased entrainment (characterized by  $C_0$ ) closer to the bar crest and larger entrainment under E2 compared to A1 (Figure 5 and tests not shown). This is consistent with the larger velocity amplitudes, larger energy and more violent breaking under E2 (and in positions closer to the bar crest).

Once sediment has been entrained, mixing processes distribute it over the water column. In regards to convective mixing, tests 34 and 51 ( $-2.8 \leq x' \leq -2.4$  m) show ripples in ACVP backscatter data. This might explain why test 51, being far offshore from the bar crest and under less energetic forcing (A1), still features a relatively wide layer of large time-averaged concentration near the bed (Figure 5d,  $\zeta' \leq 0.035$  m). Other experiments in oscillating water tunnels (Davies & Thorne, 2005) and large-scale wave flumes (van der Zanden et al., 2019b) similarly indicate wide layers of large time-averaged concentration over rippled beds. Furthermore, the influence of convective mixing processes might explain the different concentration profile shape (Figure 5) when comparing this test to the others.

Close to the bar crest and under E2, intrawave time series (Figure 6d/7d in Grossmann et al. (2022) and Figure 3d) and time-averaged concentration profiles (Figure 5) indicate larger amounts of sediment in suspension. Here, visual observations showed a planar bed so that diffusive mixing processes should dominate. Aagaard and Jensen (2013) observed a transition from diffusive mixing in the outer surf zone to convective mixing, probably induced by injected breaker vortices, in the main breaker zone. The fitted mixing parameters of the present experiments (Figure 5) show diffusive mixing of similar magnitude in most locations. This indicates limited influence from injected vortices in the present experiments up to the outer edge of the main breaker zone. But combined with the larger entrainment under E2, the diffusive mixing of similar magnitudes leads to the larger suspended concentrations. And this has important consequences on bar migration direction. Note, however, that Rouse profiles are a very simplified analysis of mixing. They are based on many assumptions and the underlying processes of sediment suspension in surf zones under ocean waves are very complex, with complicating factors like grain size (e.g., Coleman, 1970), burst and sweep events (e.g., Soldati & Marchioli, 2012), horizontal non-uniformities and advection (e.g., van der Zanden et al., 2017a) or intrawave turbulence (e.g., Aagaard et al., 2021) for example.

### 4.3. Considering Natural Beaches

Laboratory experiments often reduce natural complexity and focus on specific aspects (e.g., cross-shore transport in the present study). While this provides additional detail on studied phenomena, certain neglected complexities might have important consequences in natural beaches (e.g., 3D beach states, longshore and rip currents, and so on). Therefore, the present laboratory experiments are now put into context with field experiments.

One of the main aspects influencing the accretion and erosion of natural beaches is the phase relationship between sediment suspension and short wave offshore/onshore velocity (causing the onshore transport which, in accreting beaches, dominates over current-related offshore transport). Aagaard et al. (2018) observed the influence of different breaker types on intrawave turbulence and sediment suspension in the field. The present laboratory experiments generally confirm the in-phase relationship under plunging breakers. Yet, other influences may alter the phase relationship even under plunging breakers - for example, opposing currents (e.g., Ruessink et al., 2011). While Brinkkemper et al. (2018) observed decreased short wave-related onshore fluxes at times of larger undertow, Christensen et al. (2019) observed that undertow and infragravity wave-related currents increased sediment suspension at short wave offshore velocity phases (see their Figure 17) through bed-generated instead of injected turbulence. In the present experiments sediment re-suspension and storage in the water column were only observed in tests near the bar crest, with considerable undertow velocities and infragravity wave heights (e.g., Figure 3d  $0.25 < t/T_r < 0.35$  for A1 and Figure 7d  $0.35 < t/T_r < 0.45$  in Grossmann et al. (2022) for E2). This may result from opposing currents but could also be related to different vertical mixing characteristics (see Section 4.2.3) and increased turbulent mixing (see also Larsen et al., 2020; van der Zanden et al., 2019a).

Field experiments (e.g., Aagaard et al., 2012; Christensen et al., 2019; Ruessink et al., 1998) often struggle to measure transport very close to the bed (a few cm) because the related sediment concentrations are outside available measuring ranges. Nevertheless, the present experiments indicate that large shares of sediment transport occur there (Figure 7). This applies especially to the onshore transports, crucial for beach accretion, and indicates that historically the importance of near-bed transport might have been overlooked. Aagaard et al. (2012), for example, stressed the importance of streaming and Lagrangian (Stokes Drift) transport for accretion. In contrast, the present experiments indicate only a subordinate influence of streaming. Stokes Drift cannot be measured with the fixed instruments of the present experiments. However, concentration profiles (Figure 5) and intrawave time series of concentration (not shown for brevity) indicate little potential for large onshore transports at the high elevations above the bed where Stokes Drift would be strongest. Instead, the dominant driver for onshore near-bed transport are the short wave-related fluxes (Figure 7).

## 5. Conclusions

Sediment transport processes during onshore sandbar migration under accretive wave conditions (named A1 with  $\Omega = 1.44$ ) were investigated through large-scale laboratory experiments. A comparison to experiments with offshore-migrating bars under erosive wave conditions (named E2 with  $\Omega = 2.54$ ; analyzed in detail by Grossmann et al. (2022)) highlighted differences and similarities. Based on the results we conclude the following.

1. Under E2, morphological evolution was characterized by offshore migration of the outer and inner bar. Under the presented A1 tests, both bars migrated onshore while maintaining a constant distance between them. Other experiments featured this type of accretive morphology as well but the morphological evolution under accretive waves is more complex than under erosive waves and seems more susceptible to morphological hysteresis influence.
2. Total transport and morphological evolution mainly resulted from a balance of short wave-related onshore and current-related offshore transport. Under E2, the larger magnitudes of current-related transport resulted in bar offshore migration. Under A1, both short wave-related and current-related transport magnitudes were lower. As the reduction in current-related offshore transport was larger, onshore transport and onshore bar migration occurred.
3. Short wave-related transport occurred mainly as bedload and current-related transport mainly as suspended load. Bedload occurred very close to the bed at high flux magnitudes. Suspended fluxes generally featured lower magnitudes but sometimes occurred over larger parts of the water column with a large influence on the depth-integrated transport rate.
4. The small reduction in short wave-related, bedload onshore transport from E2 to A1 is attributed to skewness and asymmetry being effective under both. Furthermore, wave breaking influenced the cross-shore evolution

- of skewness, asymmetry and onshore transport rates. Especially asymmetry (deemed crucial for sediment transport formulations), could not be replicated well with commonly-used parametrizations.
5. The large reduction in current-related, suspended offshore transport from E2 to A1 was linked to the dissimilar effects of time-averaged currents and sediment suspension. Lower offshore currents under A1 compared to E2 were attributed to differences in wave breaking and resulting forcing mechanisms. Lower time-averaged suspension resulted from less entrainment at the bed and, potentially, less efficient mixing.
  6. Current-related onshore fluxes near the bed resulted from streaming processes within the wave boundary layer. Such fluxes were observed both under A1 and E2 in locations where offshore-directed undertow was low. The opposing influences of streaming and undertow caused complicated current-related flux profiles under A1 close to the bar crest. However, the onshore transport contributions from streaming were much lower than the ones from short waves.
  7. Because of low infragravity velocities and low sediment suspension at infragravity time scale, the influence of infragravity wave-related transport was negligible in most tests. Only during E2 on top of the bar crest, where infragravity wave height and velocity amplitude increased, the infragravity wave-related transport became notable.
  8. Identified priorities for improvement of numerical model performance under accretive wave conditions include description of sediment entrainment and mixing under complicating influences like turbulence injection, parametrizing the effects of skewness and asymmetry on near-bed orbital velocities and bedload transport, and precise determination of the breaking position.

The data presented in this article can be consulted online (see Data Availability Statement). They represent natural conditions closely while providing the measurement detail currently only possible in the laboratory. Thus, apart from providing physical insights, they may be of particular interest for the further development of (process-based) numerical models.

## Data Availability Statement

For data related to this article, visit <https://doi.org/10.5281/zenodo.6645980>.

## Acknowledgments

We thank Dr. Troels Aagaard and another, anonymous reviewer for their valuable comments which helped to improve the manuscript. The experiments described in this work were funded by the European Community's Horizon 2020 Programme through the grant to the budget of the Integrated Infrastructure Initiative HYDRALAB+, Contract 654110, and were conducted as part of the transnational access project RESIST. FG acknowledges funding from the Agency for Management of University and Research Grants (AGAUR). DH acknowledges funding from the French DGA funded ANR ASTRID Maturation project MESURE (ANR-16-ASMA-0005-01). JA acknowledges funding from the Serra Hünter Programme (SHP). We wish to thank fellow RESIST researchers and the CIEM staff (Joaquim Sospedra, Oscar Galego, Dr. Andrea Marzeddu, and Dr. Iván Cáceres) for their contributions to the experiments.

## References

- Aagaard, T., Brinkkemper, J., Christensen, D. F., Hughes, M. G., & Ruessink, G. (2021). Surf zone turbulence and suspended sediment dynamics – A review. *Journal of Marine Science and Engineering*, 9(11), 1300. <https://doi.org/10.3390/jmse9111300>
- Aagaard, T., Hughes, M., Baldock, T., Greenwood, B., Kroon, A., & Power, H. (2012). Sediment transport processes and morphodynamics on a reflective beach under storm and non-storm conditions. *Marine Geology*, 326–328, 154–165. <https://doi.org/10.1016/j.margeo.2012.09.004>
- Aagaard, T., Hughes, M. G., & Ruessink, G. (2018). Field observations of turbulence, sand suspension, and cross-shore transport under spilling and plunging breakers. *Journal of Geophysical Research: Earth Surface*, 123(11), 2844–2862. <https://doi.org/10.1029/2018JF004636>
- Aagaard, T., & Jensen, S. G. (2013). Sediment concentration and vertical mixing under breaking waves. *Marine Geology*, 336, 146–159. <https://doi.org/10.1016/j.margeo.2012.11.015>
- Aagaard, T., Kroon, A., Hughes, M., & Greenwood, B. (2008). Field observations of nearshore bar formation. *Earth Surface Processes and Landforms*, 33(7), 1021–1032. <https://doi.org/10.1002/esp.1599>
- Amoudry, L. O., Bell, P. S., Thorne, P. D., & Souza, A. J. (2013). Toward representing wave-induced sediment suspension over sand ripples in RANS models. *Journal of Geophysical Research: Oceans*, 118(5), 2378–2392. <https://doi.org/10.1002/jgrc.20188>
- Babanin, A., Chalikov, D., Young, I., & Savelyev, I. (2007). Predicting the breaking onset of surface water waves. *Geophysical Research Letters*, 34(7), L07605. <https://doi.org/10.1029/2006GL029135>
- Bagnold, R. A. (1946). Motion of waves in shallow water. Interaction between waves and sand bottoms. *Philosophical Transactions of the Royal Society of London - Series A: Mathematical and Physical Sciences*, 187, 1–18. <https://doi.org/10.1098/rspa.1946.0062>
- Baldock, T. E. (2012). Dissipation of incident forced long waves in the surf zone—Implications for the concept of “bound” wave release at short wave breaking. *Coastal Engineering*, 60, 276–285. <https://doi.org/10.1016/j.coastaleng.2011.11.002>
- Baldock, T. E., & Alsina, J. M. (2013). Impact of beach scraping on near shore sediment transport and bar migration. *Coasts and Ports 2013: 21st Australasian Coastal and Ocean Engineering Conference and the 14th Australasian Port and Harbour Conference, Manly, NSW Australia, 11–13 September 2013*.
- Baldock, T. E., Alsina, J. M., Cáceres, I., Vicinanza, D., Contestabile, P., Power, H., & Sánchez-Arcilla, A. (2011). Large-scale experiments on beach profile evolution and surf and swash zone sediment transport induced by long waves, wave groups and random waves. *Coastal Engineering*, 58(2), 214–227. <https://doi.org/10.1016/j.coastaleng.2010.10.006>
- Baldock, T. E., Birrien, F., Atkinson, A., Shimamoto, T., Wu, S., Callaghan, D. P., & Nielsen, P. (2017). Morphological hysteresis in the evolution of beach profiles under sequences of wave climates - Part 1; observations. *Coastal Engineering*, 128, 92–105. <https://doi.org/10.1016/j.coastaleng.2017.08.005>
- Bonneton, P., Lannes, D., Martins, K., & Michallet, H. (2018). A nonlinear weakly dispersive method for recovering the elevation of irrotational surface waves from pressure measurements. *Coastal Engineering*, 138, 1–8. <https://doi.org/10.1016/j.coastaleng.2018.04.005>
- Brinkkemper, J. A., Aagaard, T., de Bakker, A. T. M., & Ruessink, B. G. (2018). Shortwave sand transport in the shallow surf zone. *Journal of Geophysical Research: Oceans*, 123(5), 1145–1159. <https://doi.org/10.1029/2017JF004425>



- Cáceres, I., Alsina, J. M., van der Zanden, J., van der A, D. A., Ribberink, J. S., & Sánchez-Arcilla, A. (2020). The effect of air bubbles on optical backscatter sensor measurements under plunging breaking waves. *Coastal Engineering*, 159, 103721. <https://doi.org/10.1016/j.coastaleng.2020.103721>
- Cheng, J., & Wang, P. (2018). Dynamic equilibrium of sandbar position and height along a low wave energy micro-tidal coast. *Continental Shelf Research*, 165, 120–136. <https://doi.org/10.1016/j.csr.2018.05.004>
- Christensen, D. F., Hughes, M. G., & Aagaard, T. (2019). Wave period and grain size controls on short-wave suspended sediment transport under shoaling and breaking waves. *Journal of Geophysical Research: Earth Surface*, 124(12), 3124–3142. <https://doi.org/10.1029/2019JF005168>
- Christensen, E. D., Walstra, D. J., & Emerat, N. (2002). Vertical variation of the flow across the surf zone. *Coastal Engineering*, 45(3), 169–198. [https://doi.org/10.1016/S0378-3839\(02\)00033-9](https://doi.org/10.1016/S0378-3839(02)00033-9)
- Coleman, N. (1970). Flume studies of the sediment transfer coefficient. *Water Resources Research*, 6(3), 801–809. <https://doi.org/10.1029/WR006i003p00801>
- Cox, D. T., & Kobayashi, N. (2000). Identification of intense, intermittent coherent motions under shoaling and breaking waves. *Journal of Geophysical Research*, 105(C6), 14223–14236. <https://doi.org/10.1029/2000JC900048>
- Dally, W. R., & Dean, R. G. (1984). Suspended sediment transport and beach profile evolution. *Journal of Waterway, Port, Coastal, and Ocean Engineering*, 110(1), 15–33. [https://doi.org/10.1061/\(ASCE\)0733-950X\(1984\)110:1\(15\)](https://doi.org/10.1061/(ASCE)0733-950X(1984)110:1(15))
- Davies, A. G., & Thorne, P. D. (2005). Modeling and measurement of sediment transport by waves in the vortex ripple regime. *Journal of Geophysical Research*, 110(C5), C05017. <https://doi.org/10.1029/2004JC002468>
- Deigaard, R., Fredsøe, J., & Hedegaard, I. B. (1986). Suspended sediment in the surf zone. *Journal of Waterway, Port, Coastal, and Ocean Engineering*, 112(1), 115–128. [https://doi.org/10.1061/\(ASCE\)0733-950X\(1986\)112:1\(115\)](https://doi.org/10.1061/(ASCE)0733-950X(1986)112:1(115))
- Dibajnia, M., & Watanabe, A. (1992). Sheet flow under nonlinear waves and currents. *Coastal Engineering Proceedings*, 1, 23.
- Doering, J. C., & Bowen, A. J. (1995). Parametrization of orbital velocity asymmetries of shoaling and breaking waves using bispectral analysis. *Coastal Engineering*, 26(1–2), 15–33. [https://doi.org/10.1016/0378-3839\(95\)00007-X](https://doi.org/10.1016/0378-3839(95)00007-X)
- Dohmen-Janssen, C. M., Hassan, W. N., & Ribberink, J. S. (2001). Mobile-bed effects in oscillatory sheet flow. *Journal of Geophysical Research*, 106(C11), 27103–27115. <https://doi.org/10.1029/2000JC000513>
- Dohmen-Janssen, C. M., Kroekenstoel, D. F., Hassan, W. N., & Ribberink, J. S. (2002). Phase lags in in oscillatory sheet flow: Experiments and bed load modelling. *Coastal Engineering*, 46(1), 61–87. [https://doi.org/10.1016/S0378-3839\(02\)00056-X](https://doi.org/10.1016/S0378-3839(02)00056-X)
- Dubarbier, B., Castelle, B., Marieu, V., & Ruessink, B. G. (2015). Process-based modeling of cross-shore sandbar behavior. *Coastal Engineering*, 95, 35–50. <https://doi.org/10.1016/j.coastaleng.2014.09.004>
- Dyrh-Nielsen, N., & Sørensen, T. (1970). Some sand transport phenomena on coasts with bars. *Proceedings of the 12th International Conference on Coastal Engineering, Washington, D.C.*, (Vol. 54, pp. 855–865). <https://doi.org/10.1061/9780872620285.054>
- Eichentopf, S., Cáceres, I., & Alsina, J. M. (2018). Breaker bar morphodynamics under erosive and accretive wave conditions in large-scale experiments. *Coastal Engineering*, 138, 36–48. <https://doi.org/10.1016/j.coastaleng.2018.04.010>
- Eichentopf, S., van der Zanden, J., Cáceres, I., & Alsina, J. M. (2019). Beach profile evolution towards equilibrium from varying initial morphologies. *Journal of Marine Science and Engineering*, 7, 406. <https://doi.org/10.3390/jmse7110406>
- Eichentopf, S., van der Zanden, J., Cáceres, I., Baldock, T. E., & Alsina, J. M. (2020). Influence of storm sequencing on breaker bar and shoreline evolution in large-scale experiments. *Coastal Engineering*, 157, 103659. <https://doi.org/10.1016/j.coastaleng.2020.103659>
- Elgar, S. (1987). Relationships involving third moments and bispectra of a harmonic process. *IEEE Transactions on Acoustics, Speech, & Signal Processing*, 35(12), 1725–1726. <https://doi.org/10.1109/TASSP.1987.1165090>
- Elgar, S., & Guza, R. (1985). Observations of bispectra of shoaling surface gravity waves. *Journal of Fluid Mechanics*, 161(-1), 425–448. <https://doi.org/10.1017/S0022112085003007>
- Flick, R. E., Guza, R. T., & Inman, D. L. (1981). Elevation and velocity measurements of laboratory shoaling waves. *Journal of Geophysical Research*, 86(C5), 4149–4160. <https://doi.org/10.1029/JC086iC05p04149>
- Fromant, G., Mieras, R. S., Revil-Baudard, T., Puleo, J. A., Hurther, D., & Chauchat, J. (2018). On bedload and suspended load measurement performances in sheet flows using acoustic and conductivity profilers. *Journal of Geophysical Research: Earth Surface*, 123(10), 2546–2562. <https://doi.org/10.1029/2017JF004560>
- Gallagher, E. L., Elgar, S., & Guza, R. T. (1998). Observations of sand bar evolution on a natural beach. *Journal of Geophysical Research*, 103(C2), 3203–3215. <https://doi.org/10.1029/97JC02765>
- Garcez Faria, A. F., Thornton, E. B., Lippmann, T. C., & Stanton, T. P. (2000). Undertow over a barred beach. *Journal of Geophysical Research*, 105(C7), 16999–17010. <https://doi.org/10.1029/2000JC900084>
- Greenwood, B., & Osborne, P. (1990). Vertical and horizontal structure in cross-shore flows: An example of undertow and wave set-up on a barred beach. *Coastal Engineering*, 14(6), 543–580. [https://doi.org/10.1016/0378-3839\(90\)90034-T](https://doi.org/10.1016/0378-3839(90)90034-T)
- Grossmann, F. G., Hurther, D., van der Zanden, J., Cáceres, I., Sánchez-Arcilla, A., & Alsina, J. M. (2022). Near-bed sediment transport during offshore bar migration in large-scale experiments. *Journal of Geophysical Research: Oceans*, 127(5), e2021JC017756. <https://doi.org/10.1029/2021JC017756>
- Hasselmann, K., Munk, W., & MacDonald, G. (1963). Bispectra of ocean waves. In M. Rosenblatt (Ed.), *Proceedings of the Symposium on time series analysis* (pp. 125–139). Wiley.
- Henderson, S., & Allen, J. (2004). Nearshore sandbar migration predicted by an eddy-diffusive boundary layer model. *Journal of Geophysical Research*, 109(C6), C06024. <https://doi.org/10.1029/2003JC002137>
- Hoefel, F., & Elgar, S. (2003). Wave-induced sediment transport and sandbar migration. *Science*, 299, 1885–1887. <https://doi.org/10.1126/science.1081448>
- Holmedal, L. E., Myrhaug, D., & Eidsvik, K. J. (2004). Sediment suspension under sheet flow conditions beneath random waves plus current. *Continental Shelf Research*, 24(17), 2065–2091. <https://doi.org/10.1016/j.csr.2004.06.021>
- Hsu, T.-J., Elgar, S., & Guza, R. T. (2006). Wave-induced sediment transport and onshore sandbar migration. *Coastal Engineering*, 53(10), 817–824. <https://doi.org/10.1016/j.coastaleng.2006.04.003>
- Hurther, D., Thorne, P. D., Bricault, M., Lemmin, U., & Barnoud, J.-M. (2011). A multi-frequency Acoustic Concentration and Velocity Profiler (ACVP) for boundary layer measurements of fine-scale flow and sediment transport processes. *Coastal Engineering*, 58(7), 594–605. <https://doi.org/10.1016/j.coastaleng.2011.01.006>
- Jensen, B., Sumer, B., & Fredsøe, J. (1989). Turbulent oscillatory boundary layers at high Reynolds numbers. *Journal of Fluid Mechanics*, 206, 265–297. <https://doi.org/10.1017/S0022112089002302>
- Kassem, H., Thompson, C. E. L., Amos, C. L., & Townend, I. H. (2015). Wave-induced coherent turbulence structures and sediment resuspension in the nearshore of a prototype-scale sandy barrier beach. *Continental Shelf Research*, 109, 78–94. <https://doi.org/10.1016/j.csr.2015.09.007>



- King, D. B. (1991). *Studies in oscillatory flow bedload sediment transport*. Doctoral Thesis, University of California. Retrieved from <https://escholarship.org/uc/item/491653vx>
- Kobayashi, N., & Johnson, B. (2001). Sand suspension, storage, advection, and settling in surf and swash zones. *Journal of Geophysical Research*, 106(C5), 9363–9376. <https://doi.org/10.1029/2000jc000557>
- Kranenburg, W. M., Ribberink, J. S., Uittenbogaard, R. E., & Hulscher, S. J. M. H. (2012). Net currents in the wave bottom boundary layer: On waveshape streaming and progressive wave streaming. *Journal of Geophysical Research*, 117, F3. <https://doi.org/10.1029/2011JF002070>
- Kroon, A., Hoekstra, P., Houwman, K., & Ruessink, G. B. (1995). Morphological monitoring of a shoreface nourishment Nourtec: Experiment at Terschelling, The Netherlands. In *Proceedings of the 24th International Conference on Coastal Engineering, Kobe, Japan*. <https://doi.org/10.1061/9780784400890.162>
- Kuriyama, Y. (2002). Medium-term bar behavior and associated sediment transport at Hasaki, Japan. *Journal of Geophysical Research*, 107(C9), 3132. <https://doi.org/10.1029/2001JC000899>
- Larsen, B. E., van der A, D. A., van der Zanden, J., Ruessink, B. G., & Fuhrman, D. R. (2020). Stabilized RANS simulation of surf zone kinematics and boundary layer processes beneath large-scale plunging waves over a breaker bar. *Ocean Modelling*, 155, 101705. <https://doi.org/10.1016/j.ocemod.2020.101705>
- Lescinski, J., & Özkan-Haller, H. T. (2005). Modeling bar migration using predicted velocity time series. *Coastal Engineering*, 2729–2741. [https://doi.org/10.1142/9789812701916\\_0220](https://doi.org/10.1142/9789812701916_0220)
- Longuet-Higgins, M. S. (1953). Mass transport in water waves. *Philosophical Transactions of the Royal Society of London - Series A: Mathematical and Physical Sciences*, 245, 535–581. <https://doi.org/10.1098/rsta.1953.0006>
- Mariño-Tapia, I. J., Russel, P. E., O'Hare, T. J., Davidson, M. A., & Huntley, D. A. (2007). Cross-shore sediment transport on natural beaches and its relation to sandbar migration patterns: 1. Field observations and derivation of a transport parameterization. *Journal of Geophysical Research*, 112(C3), C03001. <https://doi.org/10.1029/2005JC002893>
- Mieras, R. S., Puleo, J. A., Anderson, D., Hsu, T.-J., Cox, D. T., & Calantoni, J. (2019). Relative contributions of bed load and suspended load to sediment transport under skewed-asymmetric waves on a sandbar crest. *Journal of Geophysical Research: Oceans*, 124(2), 1294–1321. <https://doi.org/10.1029/2018JC014564>
- Nielsen, P. (1992). *Coastal bottom boundary layers and sediment transport*. World Scientific. <https://doi.org/10.1142/1269>
- Nielsen, P., & Callaghan, D. P. (2003). Shear stress and sediment transport calculations for sheet flow under waves. *Coastal Engineering*, 47(3), 347–354. [https://doi.org/10.1016/S0378-3839\(02\)00141-2](https://doi.org/10.1016/S0378-3839(02)00141-2)
- O'Donoghue, T., & Wright, S. (2004). Flow tunnel measurements of velocities and sand flux in oscillatory sheet flow for well-sorted and graded sands. *Coastal Engineering*, 51(11–12), 1163–1184. <https://doi.org/10.1016/j.coastaleng.2004.08.001>
- O'Hara Murray, R. B., Hodgson, D. M., & Thorne, P. D. (2012). Wave groups and sediment resuspension processes over evolving sandy bedforms. *Continental Shelf Research*, 46, 16–30. <https://doi.org/10.1016/j.csr.2012.02.011>
- Padilla, E. M., & Alsina, J. M. (2017). Transfer and dissipation of energy during wave group propagation on a gentle beach slope. *Journal of Geophysical Research: Oceans*, 122(8), 6773–6794. <https://doi.org/10.1002/2017JC012703>
- Phillips, M. S., Harley, M. D., Turner, I. L., Splinter, K. D., & Cox, R. J. (2017). Shoreline recovery on wave-dominated sandy coastlines: The role of sandbar morphodynamics and nearshore wave parameters. *Marine Geology*, 385, 146–159. <https://doi.org/10.1016/j.margeo.2017.01.005>
- Rafati, Y., Hsu, T. J., Elgar, S., Raubenheimer, B., Quataert, E., & van Dongeren, A. (2021). Modeling the hydrodynamics and morphodynamics of sandbar migration events. *Coastal Engineering*, 166, 103885. <https://doi.org/10.1016/j.coastaleng.2021.103885>
- Ribberink, J. S., & Al-Salem, A. A. (1995). Sheet flow and suspension of sand in oscillatory boundary layers. *Coastal Engineering*, 25(3–4), 205–225. [https://doi.org/10.1016/0378-3839\(95\)00003-T](https://doi.org/10.1016/0378-3839(95)00003-T)
- Ribberink, J. S., van der Werf, J. J., O'Donoghue, T., & Hassan, W. N. M. (2008). Sand motion induced by oscillatory flows: Sheet flow and vortex ripples. *Journal of Turbulence*, 9, N20. <https://doi.org/10.1080/14685240802220009>
- Rocha, M. V. L., Michallet, H., & Silva, P. A. (2017). Improving the parameterization of wave nonlinearities – The importance of wave steepness, spectral bandwidth and beach slope. *Coastal Engineering*, 121, 77–89. <https://doi.org/10.1016/j.coastaleng.2016.11.012>
- Roelvink, J. A., & Stive, M. J. F. (1989). Bar-generating cross-shore flow mechanisms on a beach. *Journal of Geophysical Research*, 94(C4), 4785–4800. <https://doi.org/10.1029/JC094iC04p04785>
- Ruessink, B. G., Houwman, K. T., & Hoekstra, P. (1998). The systematic contribution of transporting mechanisms to the cross-shore sediment transport in water depths of 3 to 9 m. *Marine Geology*, 152(4), 295–324. [https://doi.org/10.1016/S0025-3227\(98\)00133-9](https://doi.org/10.1016/S0025-3227(98)00133-9)
- Ruessink, B. G., Kuriyama, Y., Reniers, A. J. H. M., Roelvink, J. A., & Walstra, D. J. R. (2007). Modeling cross-shore sandbar behavior on the timescale of weeks. *Journal of Geophysical Research*, 112, F3. <https://doi.org/10.1029/2006JF000730>
- Ruessink, B. G., Michallet, H., Abreu, T., Sancho, F., Van der A, D. A., Van der Werf, J. J., & Silva, P. A. (2011). Observations of velocities, sand concentrations, and fluxes under velocity-asymmetric oscillatory flows. *Journal of Geophysical Research*, 116(C3), C03004. <https://doi.org/10.1029/2010JC006443>
- Ruessink, B. G., Ramaekers, G., & van Rijn, L. C. (2012). On the parameterization of the free-stream non-linear wave orbital motion in nearshore morphodynamic models. *Coastal Engineering*, 65, 56–63. <https://doi.org/10.1016/j.coastaleng.2012.03.006>
- Ruiz de Alegría-Arzaburu, A., & Vidal-Ruiz, J. (2018). Beach recovery capabilities after El Niño 2015–2016 at Ensenada beach, Northern Baja California. *Ocean Dynamics*, 68(6), 749–759. <https://doi.org/10.1007/s10236-018-1164-6>
- Sleath, J. (1987). Turbulent oscillatory flow over rough beds. *Journal of Fluid Mechanics*, 182(-1), 369–409. <https://doi.org/10.1017/S0022112087002374>
- Soldati, A., & Marchioli, C. (2012). Sediment transport in steady turbulent boundary layers: Potentials, limitations, and perspectives for Lagrangian tracking in DNS and LES. *Advances in Water Resources*, 48, 18–30. <https://doi.org/10.1016/j.advwatres.2012.05.011>
- Sumer, B. M., Guner, H. A. A., Hansen, N. M., Fuhrman, D. R., & Fredsøe, J. (2013). Laboratory observations of flow and sediment transport induced by plunging regular waves. *Journal of Geophysical Research: Oceans*, 118(11), 6161–6182. <https://doi.org/10.1002/2013JC009324>
- Svendsen, I. A. (1984). Mass flux and undertow in a surf zone. *Coastal Engineering*, 8(4), 347–365. [https://doi.org/10.1016/0378-3839\(84\)90030-9](https://doi.org/10.1016/0378-3839(84)90030-9)
- Svendsen, I. A. (2005). *Introduction to nearshore hydrodynamics*. World Scientific. <https://doi.org/10.1142/5740>
- Thorne, P. D., Davies, A. G., & Bell, P. S. (2009). Observations and analysis of sediment diffusivity profiles over sandy rippled beds under waves. *Journal of Geophysical Research*, 114(C2), C02023. <https://doi.org/10.1029/2008JC004944>
- Thorne, P. D., Williams, J. J., & Davies, A. G. (2002). Suspended sediments under waves measured in a large-scale flume facility. *Journal of Geophysical Research*, 107(C8), 4–16. <https://doi.org/10.1029/2001JC000988>
- Thornton, E. B., Humiston, R. T., & Birkemeier, W. (1996). Bar/trough generation on a natural beach. *Journal of Geophysical Research*, 101(C5), 12097–12110. <https://doi.org/10.1029/96JC00209>
- Tooby, P. F., Wick, G. L., & Isaacs, J. D. (1977). The motion of a small sphere in a rotating velocity field: A possible mechanism for suspending particles in turbulence. *Journal of Geophysical Research*, 82(15), 2096–2100. <https://doi.org/10.1029/JC082i015p02096>

- Torres-Freyermuth, A., Lara, J. L., & Losada, I. J. (2010). Numerical modelling of short- and long-wave transformation on a barred beach. *Coastal Engineering*, 57(3), 317–330. <https://doi.org/10.1016/j.coastaleng.2009.10.013>
- Trowbridge, J., & Madsen, O. S. (1984). Turbulent wave boundary layers: 2. Second-Order theory and mass transport. *Journal of Geophysical Research*, 89(C5), 7999–8007. <https://doi.org/10.1029/JC089iC05p07999>
- van der A, D. A., O'Donoghue, T., Davies, A., & Ribberink, J. S. (2011). Experimental study of the turbulent boundary layer in acceleration-skewed oscillatory flow. *Journal of Fluid Mechanics*, 684, 251–283. <https://doi.org/10.1017/jfm.2011.300>
- van der A, D. A., O'Donoghue, T., & Ribberink, J. S. (2010). Measurements of sheet flow transport in acceleration-skewed oscillatory flow and comparison with practical formulations. *Coastal Engineering*, 57(3), 331–342. <https://doi.org/10.1016/j.coastaleng.2009.11.006>
- van der A, D. A., Ribberink, J. S., van der Werf, J. J., O'Donoghue, T., Buijsrogge, R. H., & Kranenburg, W. M. (2013). Practical sand transport formula for non-breaking waves and currents. *Coastal Engineering*, 76, 26–42. <https://doi.org/10.1016/j.coastaleng.2013.01.007>
- van der Zanden, J., van der A, D. A., Cáceres, I., Larsen, B. E., Fromant, G., Petrotta, C., et al. (2019a). Spatial and temporal distributions of turbulence under bichromatic breaking waves. *Coastal Engineering*, 146, 65–80. <https://doi.org/10.1016/j.coastaleng.2019.01.006>
- van der Zanden, J., van der A, D. A., Hurther, D., Cáceres, I., O'Donoghue, T., Hulscher, S. J. M. H., & Ribberink, J. S. (2017b). Bedload and suspended load contributions to breaker bar morphodynamics. *Coastal Engineering*, 129, 74–92. <https://doi.org/10.1016/j.coastaleng.2017.09.005>
- van der Zanden, J., van der A, D. A., Hurther, D., Cáceres, I., O'Donoghue, T., & Ribberink, J. S. (2017a). Suspended sediment transport around a large-scale laboratory breaker bar. *Coastal Engineering*, 125, 51–69. <https://doi.org/10.1016/j.coastaleng.2017.03.007>
- van der Zanden, J., van der A, D. A., Thorne, P. D., O'Donoghue, T., & Ribberink, J. S. (2019b). Sand suspension and fluxes by wave groups and equivalent monochromatic waves. *Continental Shelf Research*, 179, 85–104. <https://doi.org/10.1016/j.csr.2019.04.005>
- van Duin, M. J. P., Wiersma, N. R., Walstra, D. J. R., van Rijn, L. C., & Stive, M. J. F. (2004). Nourishing the shoreface: Observations and hindcasting of the Egmond case, The Netherlands. *Coastal Engineering*, 51(8–9), 813–837. <https://doi.org/10.1016/j.coastaleng.2004.07.011>
- van Enckevort, I. M. J., & Ruessink, G. B. (2003a). Video observations of nearshore bar behaviour. Part 1: Alongshore uniform variability. *Continental Shelf Research*, 23(5), 501–512. [https://doi.org/10.1016/S0278-4343\(02\)00234-0](https://doi.org/10.1016/S0278-4343(02)00234-0)
- van Enckevort, I. M. J., & Ruessink, G. B. (2003b). Video observations of nearshore bar behaviour. Part 2: Alongshore non-uniform variability. *Continental Shelf Research*, 23(5), 513–532. [https://doi.org/10.1016/S0278-4343\(02\)00235-2](https://doi.org/10.1016/S0278-4343(02)00235-2)
- van Rijn, L. C., Tonnon, P. K., & Walstra, D. J. R. (2011). Numerical modelling of erosion and accretion of plane sloping beaches at different scales. *Coastal Engineering*, 58(7), 637–655. <https://doi.org/10.1016/j.coastaleng.2011.01.009>
- Villard, P. V., Osborne, P. D., & Vincent, C. E. (2000). Influence of wave groups on SSC patterns over vortex ripples. *Continental Shelf Research*, 20(17), 2391–2410. [https://doi.org/10.1016/S0278-4343\(99\)00068-0](https://doi.org/10.1016/S0278-4343(99)00068-0)
- Walstra, D. J. R., Reniers, A. J. H. M., Ranasinghe, R., Roelvink, J. A., & Ruessink, B. G. (2012). On bar growth and decay during interannual net offshore migration. *Coastal Engineering*, 60(1), 190–200. <https://doi.org/10.1016/j.coastaleng.2011.10.002>
- Wijnberg, K., & Kroon, A. (2002). Barred beaches. *Geomorphology*, 48(1), 103–120. [https://doi.org/10.1016/S0169-555X\(02\)00177-0](https://doi.org/10.1016/S0169-555X(02)00177-0)
- Williams, J. J., Metje, N., Coates, L. E., & Atkins, P. R. (2007). Sand suspension by vortex pairing. *Geophysical Research Letters*, 34(15), L15603. <https://doi.org/10.1029/2007GL030761>
- Wright, L. D., & Short, A. C. (1984). Morphodynamic variability of surf zones and beaches: A synthesis. *Marine Geology*, 56(1–4), 93–118. [https://doi.org/10.1016/0025-3227\(84\)90008-2](https://doi.org/10.1016/0025-3227(84)90008-2)
- Yoon, H., & Cox, D. (2010). Large-scale laboratory observations of wave breaking turbulence over an evolving beach. *Journal of Geophysical Research*, 115(C10), C10007. <https://doi.org/10.1029/2009JC005748>
- Zhou, Z., Hsu, T.-J., Cox, D., & Liu, X. (2017). Large-eddy simulation of wave-breaking induced turbulent coherent structures and suspended sediment transport on a barred beach. *Journal of Geophysical Research: Oceans*, 122(1), 207–235. <https://doi.org/10.1002/2016JC011884>
- Zou, Q., Hay, A. E., & Bowen, A. J. (2003). Vertical structure of surface gravity waves propagating over a sloping seabed: Theory and field measurements. *Journal of Geophysical Research*, 108(C8), 3265. <https://doi.org/10.1029/2002JC001432>